Chemical Geology 415 (2015) 17–36

Contents lists available at ScienceDirect

Chemical Geology

journal homepage: www.elsevier.com/locate/chemgeo

Skarn xenolith record crustal CO_2 liberation during Pompeii and Pollena eruptions, Vesuvius volcanic system, central Italy

E.M. Jolis [a,*], V.R. Troll [a,b], C. Harris [c], C. Freda [b], M. Gaeta [d,b], G. Orsi [e,f], C. Siebe [g]

[a] Dept. of Earth Sciences, CEMPEG, Uppsala University, Villavägen 16, SE-752 36 Uppsala, Sweden
[b] Istituto Nazionale di Geofisica e Vulcanologia, Via di Vigna Murata 605, 00143 Roma, Italy
[c] Dept. of Geological Sciences, University of Cape Town, Rondebosch 7701, South Africa
[d] Dip. di Scienze della Terra, Sapienza Università di Roma, P.le Aldo Moro 5, 00185 Roma, Italy
[e] Dip.o di Scienze della Terra, dell'Ambiente e delle Risorse, Università degli Studi di Napoli Federico II, Largo S. Marcellino, 80138 Naples, Italy
[f] Dip. di Fisica "E. R. Caianiello" Università degli Studi di Salerno, Via Giovanni Paolo II 132, 8e4084, Fisciano, Salerno, Italy
[g] Dept. de Vulcanología, Instituto de Geofísica, UNAM, 04510 México, D.F., México

ARTICLE INFO

Article history:
Received 5 November 2014
Received in revised form 27 August 2015
Accepted 4 September 2015
Available online 7 September 2015

Keywords:
Vesuvius volcanic system
Marble and skarn xenoliths
Magma–carbonate interaction
C and O isotopes
CO_2 emission

ABSTRACT

Limestone assimilation and skarn formation are important processes in magmatic systems emplaced within carbonate-rich crust and can affect the composition of the magma and that of associated volcanic gas. In this study we focus on marble and calc-silicate (skarn) xenoliths from contact reactions between magma and carbonate wall-rock of the Vesuvius volcanic system. We present new elemental and C-O isotope data for marble and skarn xenoliths as well as for igneous rocks collected from the AD 79 (Pompeii) and AD 472 (Pollena) eruptions. The igneous samples have consistently high $\delta^{18}O$ values (9.3 to 10.8‰), but low H_2O contents (≤1.5%), indicating that magma–crust interaction prior to eruption took place. The marble xenoliths, in turn, record initial decarbonation reactions and fluid-mass exchange in their textures and $\delta^{13}C$ and $\delta^{18}O$ ranges, while the skarn xenoliths reflect prolonged magma–carbonate interaction and intense contact metamorphism. Skarn-xenoliths record Ca and Mg release from the original carbonate and uptake of Al and Si and span the full $\delta^{18}O$ data range from unmetamorphosed carbonate (>18‰) to values typical for Vesuvius magmatic rocks (~7.5‰), which implies that skarn xenoliths comprise carbonate and magmatic components. Textural and chemical evidence suggest that direct carbonate dissolution into the host magmas occurred as well as post-metamorphic skarn recycling, resulting in progressive Ca and Mg liberation from the skarn xenoliths into the magma. Magma–carbonate interaction is an additional source of CO_2 during carbonate break-down and assimilation and we calculate the amount of extra volatile components likely liberated by contact metamorphic reactions before and during the investigated eruptions. We find that the extra CO_2 added into the volcanic system could have outweighed the magmatic CO_2 component by ≥ factor seven and thus likely increased the intensity of both the Pompeii and the Pollena eruptive events.

1. Introduction

The geochemical signatures of continental magmas frequently indicate involvement of crustal components in their genesis and evolution (e.g., Hildreth and Moorbath, 1988; Davidson et al., 1990, 2005; Troll et al., 2005; Walker et al., 2007). In particular, magma–carbonate interaction has been demonstrated for a series of volcanic and plutonic systems which, like the Vesuvius volcanic system are emplaced into carbonate-rich crust (e.g., Goff et al., 2001; Wenzel et al., 2002; Dallai et al., 2004, 2011; Barnes et al., 2005; Schaaf et al., 2005; Piochi et al., 2006; Chadwick et al., 2007; Di Renzo et al., 2007; Iacono-Marziano et al., 2007, 2008; Freda et al., 2008; Gaeta et al., 2009; Deegan et al., 2010; Troll et al., 2012, 2013; Di Rocco et al., 2012; Borisova et al., 2013; Jeffery et al., 2013). A large variety of xenolith types is present in the Somma-Vesuvius eruptive products, including abundant weakly-to-highly metamorphosed carbonate and calc-silicate (skarn) type compositions. These provide unequivocal evidence for magma–carbonate interaction during magma differentiation (e.g., Fulignati et al., 2000, 2001; Gilg et al., 2001; Del Moro et al., 2001; Iacono-Marziano et al., 2008, 2009). Skarn-type calc-silicate compositions typically develop in contact-metamorphic aureoles in response to interaction between limestone or dolostone with a silicate magma. Skarn formation is known to progressively modify the composition of both the magma and the carbonate wall-rock (e.g., Gilg et al., 2001; Fulignati et al., 2004; Gaeta et al., 2009; Mollo et al., 2010; Di Rocco et al., 2012). Therefore, assessment of the textural and compositional diversity of calc-silicate xenolith assemblages can provide an opportunity to shed light on the processes at work during sub-volcanic

* Corresponding author at: Department of Earth Sciences, CEMPEG, Uppsala University, Villavägen 16, 752 36, Uppsala, Sweden.
E-mail address: ester.jolis@geo.uu.se (E.M. Jolis).

http://dx.doi.org/10.1016/j.chemgeo.2015.09.003
0009-2541/

magma–carbonate interaction in such crustal settings (Fulignati et al., 2000, 2001, 2004; Barnes et al., 2005; Chadwick et al., 2007; Gaeta et al., 2009; Di Rocco et al., 2012; Troll et al., 2013).

Previous mineralogical and geochemical studies on skarn xenoliths from the Vesuvius volcanic system characterised the pressure-temperature conditions of formation, the nature of fluids involved, and identified the principal isotopic changes associated with conversion from limestone to skarn (Fulignati et al., 2000, 2001, 2004, 2005a, 2005b; Gilg et al., 2001; Del Moro et al., 2001; Lima et al., 2007). Skarn xenoliths in the Vesuvius eruptive deposits can be linked to relatively shallow magma reservoirs (≤4–10 km; Auger et al., 2001; Civetta et al., 2004; Scaillet et al., 2008 and references therein) that were located within the thick limestone and dolostone carbonates under the volcano and which extend from approximately ≥2 km to at least 8 km depth (Zollo et al., 1996; Bruno et al., 1998; Auger et al., 2001; Pappalardo and Mastrolorenzo, 2010).

Conversely, variations of Sr-Nd-Pb-O isotopic compositions in central Italian magmas, including those from Vesuvius, have indeed been attributed by a number of workers to crustal assimilation of carbonates during storage in the upper few kilometres of the crust (e.g., Cioni et al., 1998; Fulignati et al., 2000; Auger et al., 2001; Di Renzo et al., 2007; Iacono-Marziano et al., 2008; Scaillet et al., 2008; Dallai et al., 2011; Pichavant et al., 2014), while other researchers favour isotopic variability of associated mantle sources (e.g., Cortini and Hermes, 1981; Ayuso et al., 1998; Peccerillo, 2005; Martin et al., 2012; Moretti et al., 2013). To evaluate the relative roles of source-enrichment vs. interaction between magma and crustal carbonate rocks, it appears necessary to explore the mechanism and processes of magma–crust interaction in more detail. In this respect, the skarn xenoliths in the AD 79 and AD 472 eruptions have previously been considered to reflect decarbonation of the carbonate wall-rock, but with limited direct effects on the resident magmas (Fulignati et al., 2004, 2005a, 2005b, 2011, 2013). On the other hand, magma–carbonate interaction has recently been suggested to have affected even the most primitive of Vesuvius's volcanic products (e.g., Dallai et al., 2011; Pichavant et al., 2014) and is thought to control the chemical and isotopic composition of present-day Vesuvius fumarole gas (Iacono-Marziano et al., 2009). Here we address this topic through a detailed study of the petrography, mineralogy, major and trace element geochemistry, and in particular the C and O isotope ratios of *i*) skarn-type calc-silicate xenoliths, *ii*) marble xenoliths and *iii*) igneous products (pyroclastic fragments and plutonic xenoliths) from the AD 79 and the AD 472 eruptive events. Using this integrated approach, we present a magma–carbonate interaction model that reconciles the geochemical features of the igneous samples with those of the crustal xenoliths. Moreover, we propose an easy to use formulation to quantify the potential volume of CO_2 liberated by contact metamorphic process during skarn formation relative to the volatile fraction released from the associated magma volumes, which allows us to consider consequences for resulting eruptive behaviour and style.

2. Geological background

2.1. Vesuvius volcanic system

The Vesuvius volcanic system erupts alkaline–potassic magmas of slightly silica-undersaturated K-basalt to K-trachyte compositions and highly silica-undersaturated K-tephrite to K-phonolite compositions (e.g., Santacroce et al., 2008, and references therein). The compositional and isotopic range of Vesuvius magmas has been explained by mantle source variability (e.g., Ayuso et al., 1998; Somma et al., 2001; Martin et al., 2012), differentiation and magma mixing (e.g., Turi and Taylor, 1976; Civetta et al., 1991; Cioni et al., 1995; Pappalardo et al., 1999), and through assimilation of carbonate wall-rock (e.g., Gilg et al., 2001; Del Moro et al., 2001; Piochi et al., 2006; Di Renzo et al., 2007; Dallai et al., 2011; Pichavant et al., 2014).

The Vesuvius volcanic system, one of the potentially most hazardous ones in Europe, dominates the densely-populated Neapolitan area of Southern Italy (Fig. 1) (Santacroce, 1987; Orsi et al., 2003; Cioni et al., 2008). The volcano is a moderate size stratovolcano complex (1281 m a.s.l.) and consists of the older Somma edifice and the more recent Vesuvius cone that grew within the summit caldera after the AD 79 Pompeii eruption (Fig. 1; Cioni et al., 1999; Santacroce et al., 2008). The history of the volcanic complex is characterised by at least four high-magnitude Plinian eruptions, and by several smaller events that cover a range of magnitudes and intensities (Cioni et al., 1999, 2008). The mainly effusive activity recorded for Mt. Somma, changed at about 22,000 y BP into primarily explosive activity, which is marked by the first Plinian event, the *Pomici di Base* eruption that produced K-trachyte to K-latite magmas (Bertagnini et al., 1998; Landi et al., 1999; Santacroce et al., 2008). This eruption was followed by the sub-Plinian 'Greenish Pumice' event at ca. 19,000 BP that was fed by a K-trachyte magma compositionally very similar to the *Pomici di Base* one (Cioni et al., 2003). Between these two major events, a small number of K-latitic, mostly effusive lateral eruptions took place (Santacroce, 1987; Di Renzo et al., 2007). In the following 19,000 y period, three further Plinian and sub-Plinian events occurred, each preceded by variably long repose periods, comprising the 'Mercato Pumice' eruption (8890 y BP, K-phonolite; Cioni et al., 1999; Aulinas et al., 2008; Santacroce et al., 2008; Mele et al., 2011), the 'Avellino Pumice' eruption (about 3900 y BP, K-phonolite–K-tephriphonolite; Cioni, 2000; Sulpizio et al., 2010a; b; Sevink et al., 2011; Balcone-Boissard et al., 2012), and the 'Pompeii Pumice' eruption (AD 79, K-phonolite - K-tephriphonolite; Sigurdsson et al., 1985; Cioni et al., 1995; Balcone-Boissard et al., 2012).

The present Vesuvius cone began growing after AD 79 event, during periods of open conduit activity. High-intensity, explosive eruptions continued to occur, the two largest being the sub-Plinian events of AD 472 (also known as the 'Pollena' eruption; Sulpizio et al., 2005) and AD 1631 (Bertagnini et al., 2006). The most recent period of activity (1631–1944) is characterised by summit and lateral lava effusions that are associated with mild explosive activity only (Santacroce, 1987; Arrighi et al., 2001).

2.2. Crustal lithologies

The nature of the lower crust beneath Vesuvius system is not well known. Geological and petrological studies have suggested that there may be a Hercynian basement (Scandone, 1982; Schutte, 1978; Pappalardo et al., 2002), but this still requires further investigation. The upper crust in the region, in turn, has been well characterised from outcrops and through the Trecase well site 1 deep drill hole (Brocchini et al., 2001). The uppermost part of the crust (≥2 km) is made of volcanic deposits, such as highly fractured interbedded lavas and pyroclastic materials, and volcaniclastic, marine- and fluvial sedimentary rocks of broadly Pleistocene ages (Santacroce, 1987; Zollo et al., 1996, 1998; De Matteis et al., 2000; Brocchini et al., 2001; Pappalardo and Mastrolorenzo, 2010). This ≥2 km Pleistocene succession is underlain by a ~8 km thick succession of Triassic to Cretaceous limestones and dolomites (D'Argenio et al., 1973; Ippolito et al., 1975; Barberi and Leoni, 1980; Bruno et al., 1998). While the carbonate succession is not found in the immediate surroundings of Vesuvius, the carbonate-rich lithologies are exposed in the Campanian region. There, they show a considerable compositional spectrum in, e.g., CaO (~ 31 to 55 wt.%), MgO (~ 0.8 to 21 wt.%) and Sr (~ 41 to 1000 ppm), $^{87}Sr/^{86}Sr$ (0.7072 to 0.70927), $\delta^{18}O$ (29 to 33‰), and $\delta^{13}C$ (−4.5 to 0.95‰) (e.g., Civetta et al., 1991; Di Renzo et al., 2007; Del Moro et al., 2001; Fulignati et al. 2005a; Piochi et al., 2006; Iannace et al., 2011; Jolis et al., 2013), which we use to assess the range of potential crustal assimilation end-members in Section 6.

The shallow magma chambers that fed the AD 79 and AD 472 eruptions have been located between 7–8 km and 3–4 km depth, respectively (e.g., Scaillet et al., 2008). This falls within the depth of

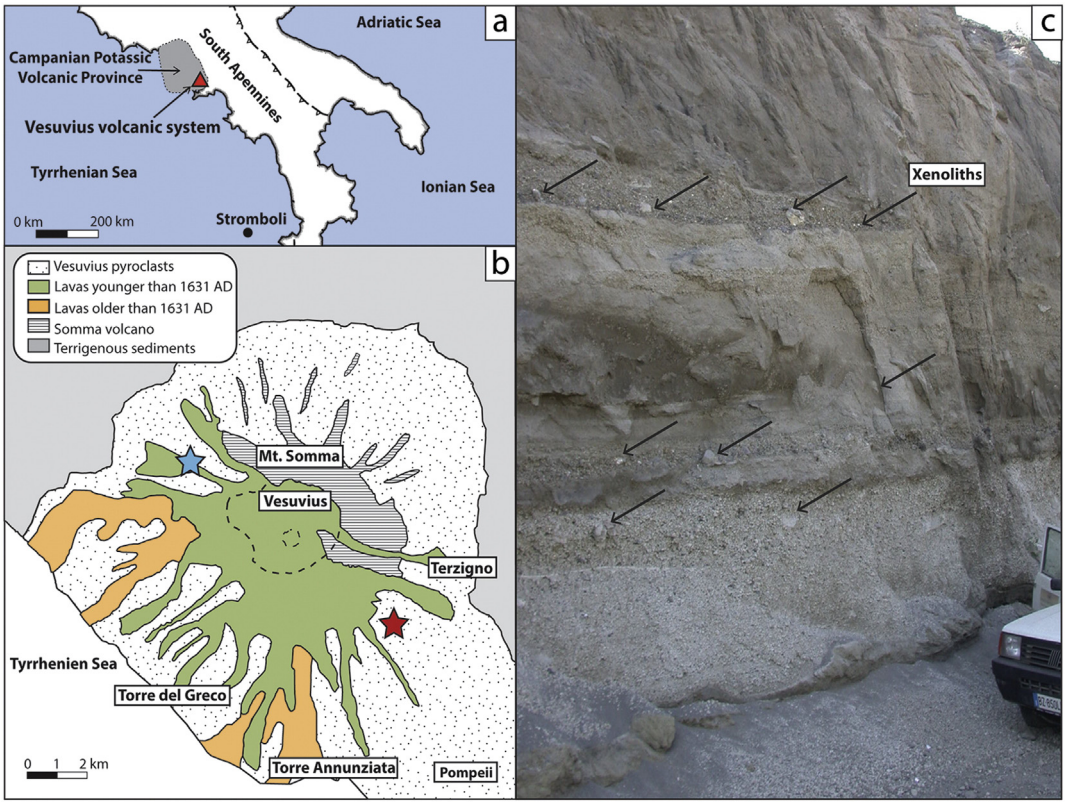

Fig. 1. a) Sketch map of Italy with the Campanian Potassic Volcanic Province (grey field) and the Vesuvius volcanic system (red triangle) indicated. b) Simplified geological map of the Vesuvius volcanic system, comprising the older Mt. Somma edifice and the younger Vesuvius cone (after Peccerillo, 2005). The stars show the sampling locations: blue star – Pollena (AD 472) and red star - Pompeii (AD 79). c) Field appearance of the Pompeii deposit at main sample site (September 2008). Note the abundance and size of marble and skarn xenoliths within the outcrop (black arrows).

the crust occupied by the Mesozoic carbonate platform (Santacroce, 1987; Barberi et al., 1981; Fulignati et al., 1998; Brocchini et al., 2001; Del Moro et al., 2001; Auger et al., 2003; Civetta et al., 2004; Del Pezzo et al., 2006) and the wall-rocks available to the magma reservoirs of these two events were thus dominantly limestones and dolostones of the Mesozoic (Triassic-Cretaceous) succession.

3. Analytical methods

A total of 53 rock samples, including igneous compositions and particularly crustal and contact-metamorphic xenoliths (marble and skarn) were collected in summer 2008 from the pyroclastic sequences of the AD 472 (Pollena) and the AD 79 (Pompeii) eruptions (Fig. 1). The crustal xenolith samples were usually between 4 and 20 cm across and encompass the full lithological spectrum from marbles to skarns. Igneous samples include juvenile pumice clasts as well as syenite and pyroxenite plutonic inclusions or xenoliths that occur embedded in the pyroclastic deposits. A description of the main characteristics of each group is provided in Section 4 and a summary table of the main petrological features of representative samples is given in Supplementary Material 1.

Major- and trace-element concentrations of 21 whole-rock samples were determined by X-ray fluorescence (XRF) at IFM-Geomar, Kiel, Germany. Samples were analysed on fused beads using an automated Philips PW1480 spectrometer equipped with a Rh-tube. Calibration was performed using international reference materials JR-1 (rhyolite), JA-2 (andesite), JB-2 and JB-3 (basalt) and standard analyses are reported in Abratis et al. (2002). Accuracy of standard measurements is <1.8% for SiO_2, TiO_2, Al_2O_3, Fe_2O_3, MnO, CaO, K_2O and P_2O_5 and <10% for MgO and Na_2O. Water and CO_2 concentrations were measured upon ignition of powders at 1200 °C using a Rosemount CWA 5003 infrared photometer (e.g., Troll and Schmincke, 2002).

Oxygen and carbon isotope ratios on 31 whole-rock samples were determined off-line using a Thermo DeltaXP mass spectrometer at the University of Cape Town (UCT), South Africa and are reported in the standard δ-notation, where $\delta = (R_{sample}/R_{standard} - 1) \times 1000$, and $R = {}^{18}O/{}^{16}O$ or ${}^{13}C/{}^{12}C$. For O-isotopes, ~10 mg powdered samples was dried in an oven at 50 °C and degassed under vacuum on a conventional silicate line at 200 °C. Silicates were reacted with ClF_3 (Borthwick and Harmon, 1982) and the liberated O_2 was converted to CO_2 using a hot platinised carbon rod (Vennemann and Smith, 1990; Harris and Ashwal, 2002; Fagereng et al., 2008). Samples were run on the vacuum line along with duplicate samples of the internal quartz standard NBS-28 that calibrates the raw data to the SMOW scale (Standard Mean Ocean Water; e.g., Sharp, 2007), using the $\delta^{18}O$ value of 9.64‰ for NBS-28 recommended by Coplen et al. (1983). During the course of this study, 19 analyses of NBS-28 gave a 2σ error of 0.16‰.

The measurement of carbon and oxygen isotope ratios of carbonate minerals (n = 12) and selected skarn samples (n = 10) was determined on CO_2 produced by reaction of whole-rock powders with 100% phosphoric acid (McCrea, 1950). Samples were reacted overnight at 50 °C and analyses are of total carbonate present. The dominant carbonate mineral present was calcite, hence the calcite-phosporic acid fractionation factor (1.009) was used in the correction procedure. Data were normalised to the SMOW and PDB scales, respectively, by using an internal standard NM95 calibrated against NBS-19 ($\delta^{18}O$ 25.10‰, $\delta^{13}C$ 1.57‰). Repeated analyses of this internal standard during this study (n = 10) gave a 2σ error of 0.05‰ and 0.09‰ for $\delta^{18}O$ and $\delta^{13}C$, respectively.

4. Sample descriptions

4.1. Crustal and contact-metamorphic xenoliths

4.1.1. Marbles

Marble fragments (n = 13) from both eruptive units are angular to rounded, and usually white, grey or yellowish in colour. They generally display equigranular crystals of calcite and occasional olivine with granoblastic–polygonal, granoblastic–interlobate, or poikiloblastic textures. In most marbles, crystals range from very fine (<0.1 mm) to fine (up to 1 mm) in grain size. One sample (V-M-21) shows coarser calcite (up to 10 mm) and also contains olivine crystals up to 1 mm in size (olivine marble; Fig. 2a). The marbles derive from thermally affected limestone or dolostone that has undergone recrystallisation and, in part, devolatilisation, but overall reflecting relatively modest interaction with metasomatic fluids or silicate melts (cf. Gilg et al., 2001).

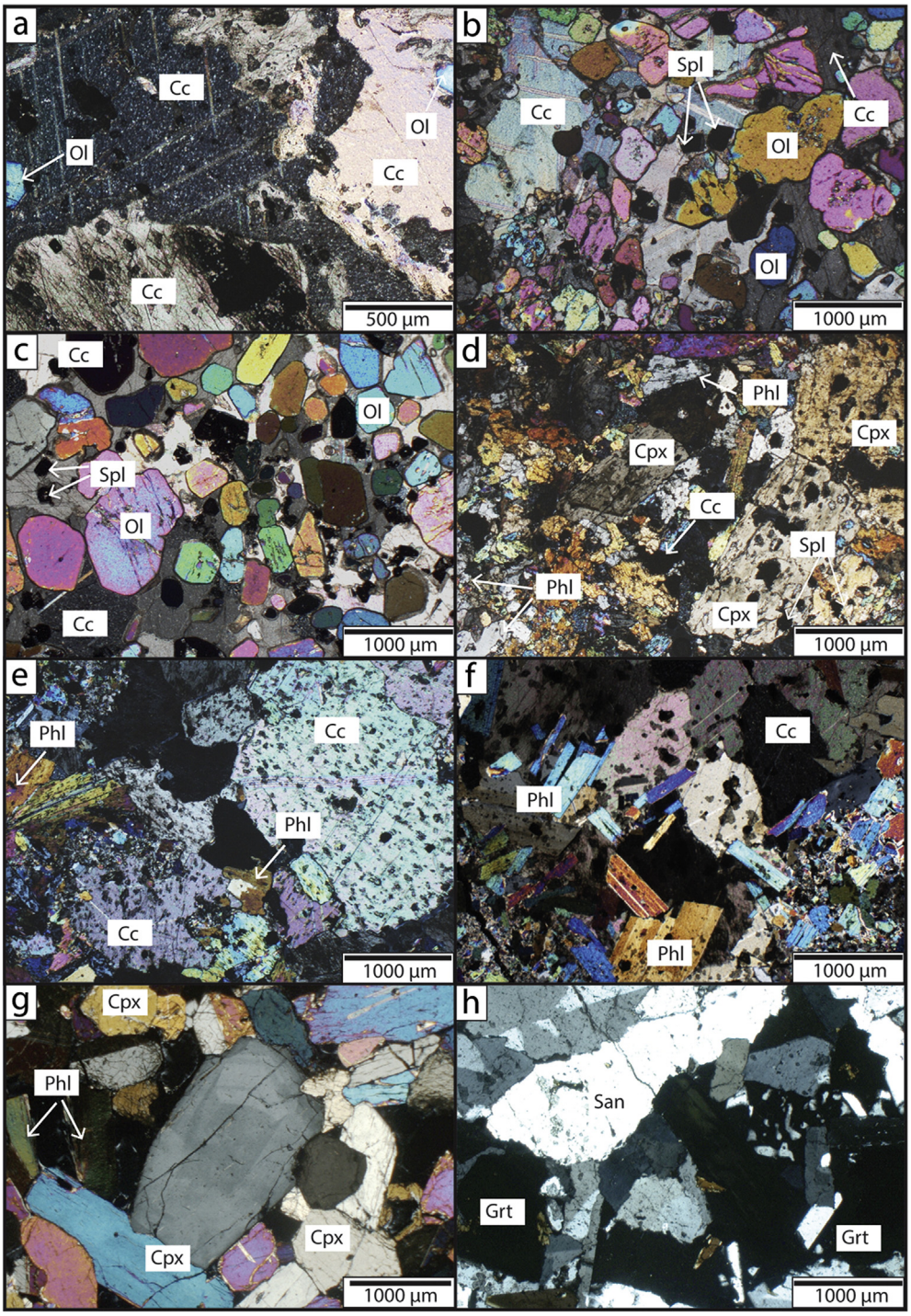

Fig. 2. Photomicrographs (CPL) of representative samples. a) Olivine-marble with submillimeter-sized olivine crystals. b & c) Olivine skarn showing intergrown fine-to-medium grained olivine, calcite, and spinel. d) Clinopyroxene-skarn with hypidioblastic texture of clinopyroxene and phlogopite. e & f) Different facies of phlogopite skarn with equigranular crystals in a decussate texture. g) Hypidiomorphic clinopyroxene and phlogopite in pyroxenite. h) Syenite with subhedral to anhedral sanidine (grey and white) and garnet (black). Abbreviations: *Cc*: calcite; *Cpx*: clinopyroxene; *Grt*: garnet; *Ol*: olivine; *Phl*: phlogopite; *Spl*: spinel; *San*: sanidine.

Table 1
Major and trace elements of representative rocks types from the Vesuvius AD 79 and AD 472 eruptions.

	Igneous rocks					Crustal xenoliths				
Sample ID	V-P-1	V-Cp-10	V-Cp-33b	V-S-27	V-S-31a	V-CS-9a	V-CS-12b	V-CS-12d	V-CS-3b	V-CS-7b
Formation	79 AD	79 AD	79 AD	472 AD	472 AD	79 AD	79 AD	79 AD	79 AD	79 AD
Rock type	pumice	phl-clinopyroxenite	clinopyroxenite-phl	syenite	syenite	skarn	skarn	skarn	skarn breccia	skarn breccia
Major elements in wt.%										
SiO_2	51.94	49.44	40.82	54.41	55.85	44.53	40.86	43.49	12.05	6.72
TiO_2	0.46	1.06	0.99	0.15	0.37	0.35	0.54	0.45	0.14	0.09
Al_2O_3	18.8	5.8	13.79	22.96	19.23	13.21	13.90	14.88	3.89	2.26
Fe_2O_3	4.64	5.88	9.33	2.54	4.07	3.74	5.66	4.36	1.29	0.72
MnO	0.14	0.08	0.08	0.19	0.26	0.06	0.16	0.05	0.04	0.02
MgO	2.15	17.18	17.93	0.09	0.32	13.55	6.80	10.81	14.59	14.65
CaO	6.06	17.7	7.47	2.63	5.37	21.11	14.31	24.19	30.51	38.84
Na_2O	4.42	0.41	0.41	8.67	5.06	0.35	2.36	0.41	0.52	0.24
K_2O	8.54	2.36	6.75	7.81	9.54	1.81	6.87	0.58	2.52	0.62
P_2O_5	0.23	0.06	0.06	0.02	0.03	0.03	0.79	0.04	0.13	0.11
Sum*	99.22	100.03	97.86	99.49	100.12	98.98	98.42	99.51	100.93	99.39
$H_2O^{\dagger}$	1.51	0.05	0.21	0.02	0.02	0.12	0.29	0.10	0.91	0.57
$CO_2^{\ddagger}$	0.33	0.01	0.02	0	0	0.12	5.88	0.15	34.34	34.55
Trace elements in ppm										
Co	2	38	33	–	1	8	10	10	6	7
Cr	36	523	0	–	–	3	50	15	–	5
Ni	1	266	53	–	–	19	14	18	33	22
V	111	265	266	13	71	78	152	71	53	58
Zn	75	29	44	129	62	37	110	32	33	25
Ce	148	–	13	277	155	71	170	59	39	0
La	170	–	31	269	194	–	153	3	–	17
Nb	57	7	24	109	103	17	50	17	18	–
Ga	16	3	14	25	23	10	14	13	3	3
Pb	46	7	9	63	50	5	17	5	25	21
Pr	22	1	5	36	26	2	21	1	0	4
Rb	349	145	378	479	402	121	279	30	139	44
Ba	963	1224	3548	12	8	1338	1210	354	303	241
Sr	772	112	124	35	230	177	882	222	683	3096
Th	34	–	5	81	61	3	15	5	11	2
Y	17	2	–	–	48	7	15	14	3	–
Zr	264	39	95	477	622	68	163	76	86	47

	Crustal xenoliths										
Sample ID	V-CS-9d	V-CS-9e	V-CS-26	V-CS-14	V-CS-16	V-CS-19	V-CS-30	V-CS-28	V-CS-25	V-M-8a	V-M-23
Formation	79 AD	79 AD	472 AD	472 AD	472 AD	472 AD	472 AD	472 AD	472 AD	79 AD	472 AD
Rock type	skarn	skarn	skarn	skarn	skarn	skarn	skarn	skarn	skarn	marble	marble
Major elements in wt.%											
SiO_2	32.06	21.19	40.44	34.02	22.87	33.87	24.24	9.30	34.44	2.48	0.30
TiO_2	0.35	0.15	0.59	0.08	0.13	0.05	0.11	0.08	0.52	0.04	0.01
Al_2O_3	14.03	7.91	15.58	4.63	7.40	2.95	8.42	4.65	11.05	0.87	0.06
Fe_2O_3	4.16	1.20	3.93	4.13	1.43	4.34	1.39	1.84	4.46	0.27	0.01
MnO	0.11	0.09	0.05	0.71	0.06	0.87	0.06	0.16	0.10	0.03	–
MgO	26.19	14.21	17.10	30.06	29.78	36.01	33.57	18.92	20.68	17.63	2.17
CaO	10.5	26.35	15.78	17.54	19.83	15.74	16.58	35.03	16.95	34.95	53.56
Na_2O	0.24	0.24	0.25	0.21	0.18	0.15	0.14	0.17	0.24	0.16	0.19
K_2O	2.83	4.93	3.29	2.27	0.42	1.64	0.29	0.01	2.78	0.17	0.02
P_2O_5	0.04	0.12	0.03	0.13	0.02	0.12	0.02	0.02	0.02	0.02	0.04
Sum*	97.34	98.35	97.69	97.86	102.2	96.89	104.31	97.15	98.27	101.04	99.9
$H_2O^{\dagger}$	1.53	0.97	0.18	0.04	0.11	0.06	0.13	0	0.71	0.03	0.02
$CO_2^{\ddagger}$	5.3	20.99	0.47	8.38	14.66	8.51	12.2	28.09	6.2	44.39	43.52
Trace elements in ppm											
Co	7	7	4	12	1	15	2	7	8	5	6
Cr	14	–	0	–	–	–	9	–	–	–	–
Ni	28	22	13	13	6	36	12	9	20	14	10
V	67	78	74	45	26	31	23	23	68	17	12
Zn	83	59	63	249	69	275	87	630	46	20	3
Ce	9	177	56	98	20	129	–	62	39	0	0
La	–	165	0	57	10	44	–	15	0	–	0
Nb	15	85	17	46	11	29	3	57	15	8	15
Ga	12	5	13	6	7	3	9	12	8	–	1
Pb	7	18	5	6	4	5	7	12	5	16	11
Pr	–	22	–	9	2	7	–	4	–	1	–
Rb	86	258	189	228	29	167	25	3	217	14	5
Ba	1281	2076	1654	26	72	3	39	–	759	18	9
Sr	481	751	170	53	216	53	163	136	140	212	499

(continued on next page)

Table 1 (*continued*)

	Crustal xenoliths										
Sample ID	V-CS-9d	V-CS-9e	V-CS-26	V-CS-14	V-CS-16	V-CS-19	V-CS-30	V-CS-28	V-CS-25	V-M-8a	V-M-23
Formation	79 AD	79 AD	472 AD	472 AD	472 AD	472 AD	472 AD	472 AD	472 AD	79 AD	472 AD
Rock type	skarn	skarn	skarn	skarn	skarn	skarn	skarn	skarn	skarn	marble	marble
Trace elements in ppm											
Th	7	15	5	10	6	3	–	3	1	5	7
Y	4	7	5	–	1	–	–	4	–	5	3
Zr	92	141	204	135	140	65	50	–	169	24	19

Sum* = total of major elements expressed as oxide. "-" indicates that the analysis was below detection limit. †CO_2 and H_2O were measured independently using an IR photometer.

4.1.2. Skarns

Skarn xenoliths (n = 28) are widespread in both deposits. They display a variety of calc-silicate mineral assemblages, sometimes with a composite nature, e.g., preserving transitions from marble to skarn or from skarn to igneous rock. Crystal size ranges from <0.1 mm up to 5 mm. Zoning and metasomatic fronts (skarn layers) are recorded by changes in modal proportions of clinopyroxene, olivine, phlogopite, and calcite, with frequent spinel and plagioclase, and rare vesuvianite, garnet, and hematite as accessory minerals. Using the most abundant mineral phases, we have subdivided the skarn samples into three

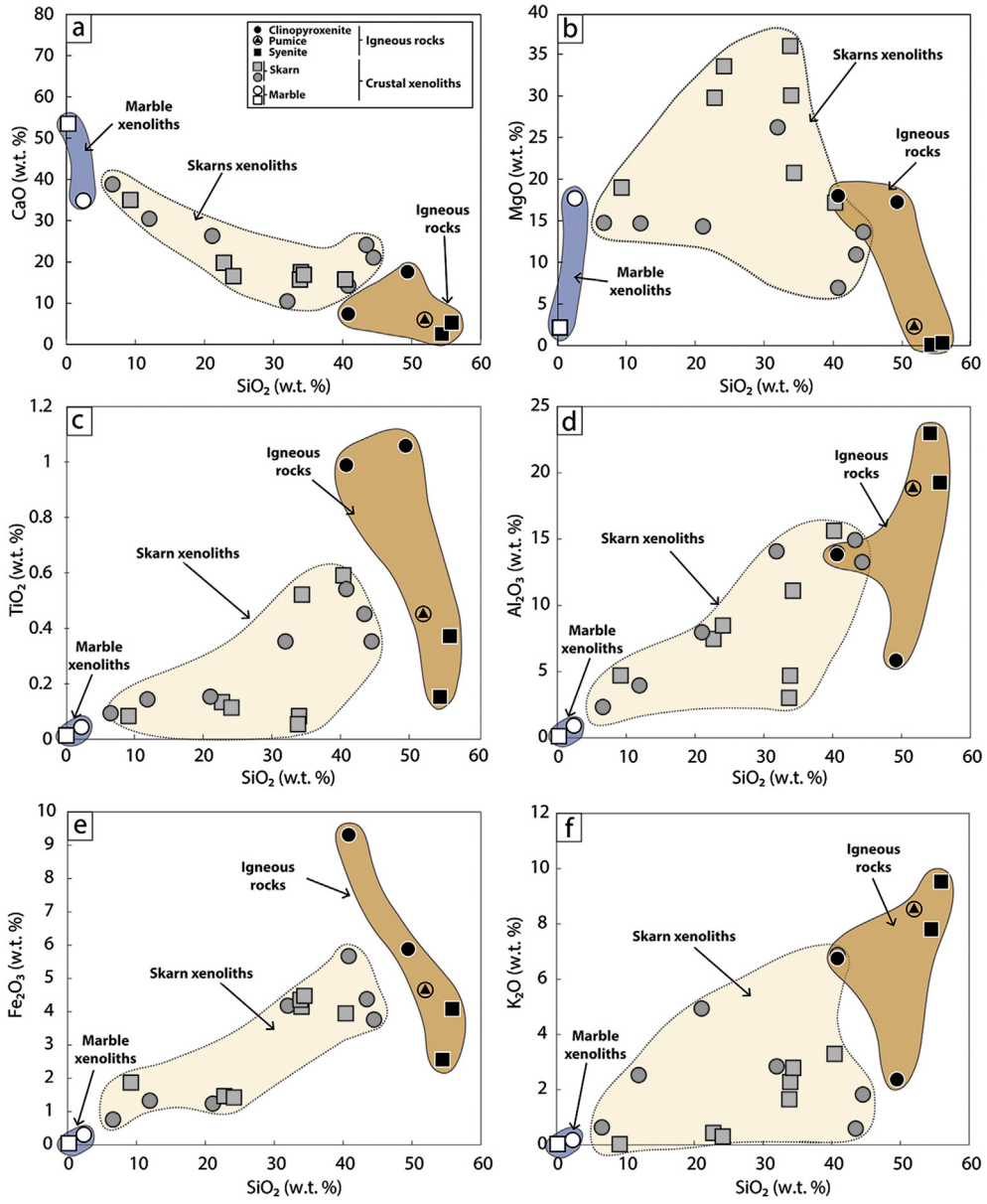

Fig. 3. Selected major element variations against SiO_2 (wt.%). The squares represent samples from the Pollena (AD 472) eruption, while the circles denote samples from the Pompeii (AD 79) eruption. The fields and rock types are: marbles = white symbols and blue field; skarns = grey symbols and yellow field; igneous rocks = black symbols and orange field.

broad classes: a) olivine-skarn, mainly showing poikilitic textures (Fig. 2b-c), b) clinopyroxene-skarn, with a hypidioblastic texture and calcite as an accessory phase (Fig. 2d), and c) phlogopite-skarn, with equigranular crystals of phlogopite and calcite in usually random orientation (decussate texture) and with variable amounts of accessory spinel (Fig. 2e).

Two skarn breccia xenoliths were collected from the AD 79 deposits (samples V-CS-3b and V-CS-7b). These breccias are composed of unsorted calcite clasts with highly variable grain sizes (from <0.1 mm to 10 mm). Calcite is associated with clinopyroxene and plagioclase and mica with hematite is frequently present as a secondary phase in between clasts. The breccia samples attest to locally intense gas fracturing and metasomatic alteration.

Two skarn xenoliths from the Pompeii eruption preserve a contact zone between an igneous and a metamorphic/metasomatic domain (V-CS-11ba and V-CS-12b). These contact areas are made up of very fine (<0.1 mm) dark and light micas. The igneous domain is in both cases characterised by a hypidiomorphic texture and a fine to medium (0.1 to 5 mm) grain size, with sanidine, amphibole, clinopyroxene, and biotite ± garnet ± titanite ± apatite ± plagioclase ± dark spinel as accessories and classifies as sanidine syenite. The metamorphic/metasomatic domains are characterised by very fine to fine grain size (< 0.1 to 1 mm) with phlogopite and calcite as the main minerals (phlogopite skarn), and apatite as an accessory phase set in a decussate texture (Fig. 2f).

4.2. Igneous compositions

The igneous samples recovered from the pyroclastic deposits can be subdivided into plutonic (or hypabyssal) rocks vs pyroclastic rocks and comprise samples from the Pompeii and the Pollena eruptions. The plutonic xenoliths (n = 6) are pyroxenites and alkali syenite with fine to medium grain sizes (0.1–5 mm) and holocrystalline to hypidiomorphic textures. The pyroxenites are characterised by high proportions of clinopyroxene with only localised domains of phlogopite (Fig. 2g), implying that these rocks are likely of cumulate origin. The alkali syenites are fine to medium grained (0.1–5 mm) and are dominated by subhedral to anhedral sanidine, garnet, and subordinate amphibole, sodalite group minerals and occasional epidote (Fig. 2h). Syenite xenoliths were only sampled from the AD 472 eruption, but their presence has been reported from several other Vesuvius eruptive units previously. They have been interpreted as part of a crystallising magmatic 'mush' at the upper margin of the magma chamber system (Fulignati et al., 2001, 2005b; Fulignati and Marianelli, 2007).

Pumice clasts investigated (n = 3) are porphyritic with crystals varying in size from <0.1 to 10 mm. Sanidine, clinopyroxene, and dark mica are the main mineral phases with plagioclase, garnet and spinel present in accessory proportions. The glassy groundmass contains both non-connected and connected vesicles that vary from ≤20 to 500 μm in size and from spherical through ovoidal, to elongated in shape.

5. Results

5.1. Major elements

Selected major element oxide, trace element, and total volatile concentrations of the discussed rock types are reported in Table 1. Whole-rock analyses show a wide range in SiO_2 and CaO contents that corroborate a subdivision into two main groups: igneous samples and crustal xenoliths (Fig. 3).

The syenites and pumices are characterised by relatively high SiO_2, Na_2O, K_2O and Al_2O_3 contents, but low CaO and MgO relative to most Vesuvian rocks, and are representative of evolved Vesuvian magmas. The compositional range reflects the presence of mainly K-feldspar (sanidine) with minor plagioclase and mafic minerals (Table 2). Clinopyroxenite samples, in turn, are gabbroic to foiditic in composition and have low SiO_2, Na_2O, K_2O and Al_2O_3 and high CaO and MgO compared to the pumice and syenite samples, consistent with abundant clinopyroxene in these rocks (Table 2).

Skarn and marble xenoliths are characterised by a broad compositional spectrum (Table 1), with SiO_2 ≤2.5 wt.% in the marbles, but with between 6.7 and 44.5 wt.% in the skarn xenoliths. Variation diagrams against SiO_2 define semi-linear trends for CaO, TiO_2, Fe_2O_3, Al_2O_3 and K_2O, while MgO concentrations in the skarn suite are more scattered. Marbles are characterised by low contents in all major element oxides except CaO and MgO, reflecting the presence of calcite and olivine. The skarns, in turn, show a larger compositional range with variable Al_2O_3, SiO_2, MgO and CaO, owing to the occurrence of variable amounts of spinel, clinopyroxene, olivine, phlogopite and calcite in their mineral assemblage (Table 2). In this respect, we note that the skarn xenoliths plot between the marble xenoliths and the igneous compositions on all variation plots (Fig. 3), except for the high MgO values preserved in some of our skarn samples. The lack of systematic

Table 2
Relationship between petrological and geochemical groups.

Sample information			Mineral phases													
Sample ID	Formation	Rock type	Cc	Ol	Spl	Phl	Plg	Cpx	Hem	San	Amp	Sodl.	Grt	Ep	Bt	Ttn	Ap
Igneous rocks																	
V-Cp-10	AD 79	phl-clinopyroxenite				√		√									
V-Cp-33b	AD 79	clinopyroxenite-phl				√		√									
V-P-1	AD 79	pumice			√		√	√		√			√		√		
V-S-27	AD 472	syenite								√	√	√	√	√			
V-S-31a	AD 472	syenite								√	√	√	√				
Crustal xenoliths																	
V-CS-3b	AD 79	skarn breccia	√				√		√						√		
V- CS-7b	AD 79	skarn breccia	√					√							√		
V-CS-9d	AD 79	skarn	√	√		√		√									
V-CS-12b	AD 79	skarn			√		√	√		√	√		√		√	√	√
V-CS-14	AD 472	skarn	√	√		√		√									
V-CS-16	AD 472	skarn	√	√	√	√											
V-CS-19	AD 472	skarn	√	√													
V-CS-26	AD 472	skarn	√	√	√	√		√									
V-CS-28	AD 472	skarn	√	√	√		√										
V-CS-30	AD 472	skarn	√	√	√	√											
V-M-8a	AD 79	marble	√														
V-M-23	AD 472	marble	√														

Cc: calcite, Ol: olivine, Spl: spinel, Phl: phlogopite, Plg: plagioclase, Cpx: clinopyroxene, Hem: hematite, San: sanidine, Amp: amphibole, Sodl: sodalite group, Grt: garnet, Ep: epidote, Bt: Biotite, Ttn: titanite, Ap: apatite.

trend for MgO against SiO_2 suggests a combination of limestone and dolostone protoliths (see Section 2.2 Crustal lithologies).

5.2. Trace elements

Whole-rock trace element concentrations are reported in Table 1 and a selection of elements is plotted against CaO wt.% in Fig. 4. The igneous samples form a broadly linear array with respect to their Zr, Rb, Nb, Th, and V concentrations, similar to most of the evolved Vesuvian lavas (e.g., Civetta et al., 1991; Ayuso et al., 1998; Somma et al., 2001). Clinopyroxenites, however, show variable trace element contents that are intermediate between the igneous syenite and pumice samples on the one side and the skarn xenoliths on the other. Additionally, high concentrations of Ni and V, but variable Cr (0–523 ppm) in these samples corroborate the presence of clinopyroxene as the main mineral phase. Incompatible element concentrations (Ce, La, Nb) are generally low, but concentrations of Ba, Rb, and Sr are relatively high, likely reflecting the variable proportions of phlogopite present in this group (Table 2).

Trace element arrays are scattered for the skarn xenoliths but broadly negative trends appear to exist for Zr, Rb, Nb, Th, and V when plotted against CaO (Fig. 4b-f). The concentrations of Cr, Ni, and Co are low in the skarn samples, whereas Rb, Sr, Zr, and Ba are high relative to the igneous samples. The higher Sr concentrations amongst the skarn samples are usually associated with the occurrence of plagioclase and/or remnant calcite in the mineral assemblage (Fig. 4a and Table 2).

5.3. Isotope data

Table 3 reports the full dataset of $\delta^{18}O$ and $\delta^{13}C$ for the igneous samples, the marble and skarn xenoliths, and the values from individual skarn layers. Fig. 5 shows the $\delta^{18}O$ and $\delta^{13}C$ values of crustal xenoliths and igneous compositions compared with mantle, crustal carbonate, and skarn data available from the literature (e.g., Ayuso et al., 1998; Gilg et al., 2001; Del Moro et al., 2001; Fulignati et al., 2005a; Scheibner et al., 2007). The $\delta^{18}O$ values of the igneous samples range from 7.5 to 12.6‰ and are considerably higher than typical mantle values ($\delta^{18}O$ = 5.7–6‰; Ito et al., 1987; Eiler et al., 1996), but overlap with Vesuvian magmatic garnets recently described (6.8–8.5‰; Scheibner et al., 2007).

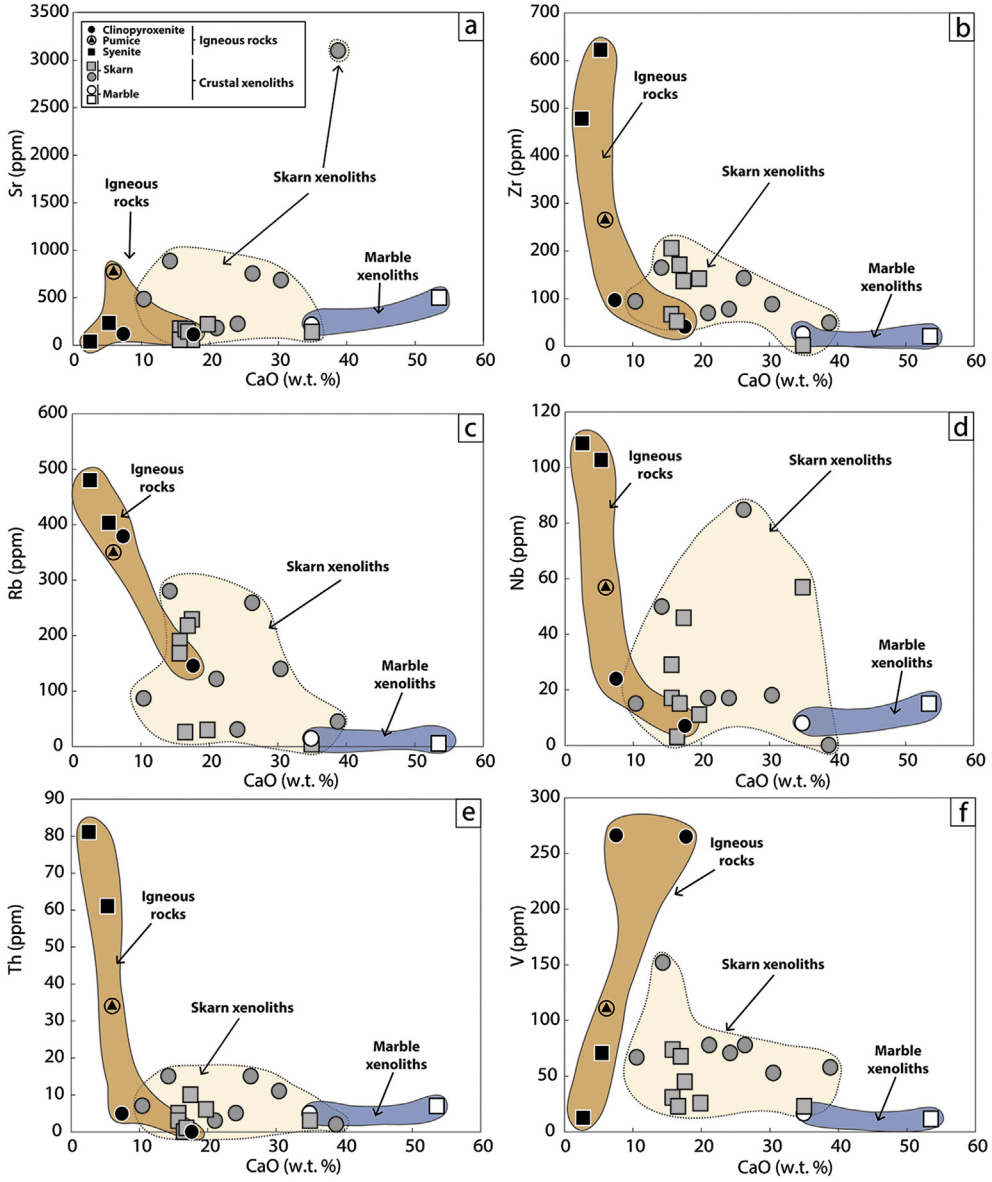

Fig. 4. Selected trace element variation diagrams against CaO (wt.%). Note, the skarn samples fall consistently in between the marbles and the igneous rocks. Symbols and fields as in Fig. 3 (see text for details).

Table 3
$\delta^{13}C$ and $\delta^{18}O$ data of rock types from the Vesuvius AD 79 and AD 472 eruptions.

Sample information			$\delta^{18}O$ ‰	$\delta^{13}C$ ‰ (carb.)	$\delta^{18}O$ ‰ (carb.)
Sample ID	Formation	Rock type			
Igneous rocks					
V-P-$1_{w.r.}$	AD 79	pumice	9.7	–	–
V-P-$33a_{w.r.}$	AD 79	pumice	10.5	–	–
V-P-$17_{w.r.}$	AD 472	pumice	9.3	–	–
V-Cp-$9b_{w.r.}$	AD 79	clinopyroxenite	8.1	–	–
V-Cp-$10_{w.r.}$	AD 79	clinopyroxenite	7.5	–	–
V-Cp-$33b_{w.r.}$	AD 79	clinopyroxenite	8.6	–	–
V-Cp-$31b_{w.r.}$	AD 472	clinopyroxenite	7.9	–	–
V-S-$27_{w.r.}$	AD 472	syenite	10.3	–	–
V-S-$31a_{w.r.}$	AD 472	syenite	10.8	–	–
Crustal xenoliths					
V-CS-$2b_{w.r.}$	AD 79	skarn	12.2	–	–
V-CS-$3b_{w.r.}$	AD 79	skarn breccia	16.3	–	–
V-CS-$3b_1$			14.9		
V-CS-$3b_2$			24.7		
V-CS-$4_{w.r.}$	AD 79	skarn	9.5	–	–
V-CS-$7a_{w.r.}$	AD 79	skarn	10.8	–	–
V-CS-$7b_{w.r.}$	AD 79	skarn breccia	–	−1.3	20.9
V-CS-$7b_1$	AD 79	skarn breccia	17.2	–	–
V-CS-$7b_2$	AD 79	skarn breccia	24.7	–	–
V-Cs-$7c_{w.r.}$	AD 79	skarn	11.9	–	–
V-CS-$7d_{w.r.}$	AD 79	skarn	–	−2.1	14.1
V-CS-$7f_{w.r.}$	AD 79	skarn	–	−1.4	17.6
V-CS-$8b_{w.r.}$	AD 79	skarn	12.6	–	–
V-CS-$9a_{w.r.}$	AD 79	skarn	9.9	–	–
V-CS-$9c_{w.r.}$	AD 79	skarn	10.6	–	–
V-CS-$9d_{w.r.}$	AD 79	skarn	18.6	–	–
V-CS-$9e_{w.r.}$	AD 79	skarn	–	−2.3	16.9
V-CS-$11a_{w.r.}$	AD 79	skarn	10.9	–	–
V-CS-$12b_{w.r.}$	AD 79	skarn	10.1	–	–
V-CS-$12c_{w.r.}$	AD 79	skarn	–	−4.5	21.5
V-CS-$12d_{w.r.}$	AD 79	skarn	10.2	–	–
V-CS-$13_{w.r.}$	AD 472	skarn	13.0	–	–
V-CS-$14_{w.r.}$	AD 472	skarn	9.7	–	–
V-CS-14_1	AD 472	skarn	11.7	–	–
V-CS-14_2	AD 472	skarn	9.1	–	–
Crustal xenoliths					
V-CS-$16_{w.r.}$	AD 472	skarn	–	−1.1	17.9
V-CS-16_1	AD 472	skarn	15.9	–	–
V-CS-16_2	AD 472	skarn	14.8	–	–
V-CS-16_3	AD 472	skarn	15.9	–	–
V-CS-$19_{w.r.}$	AD 472	skarn	11.1	–	–
V-CS-19_1	AD 472	skarn	11.3	–	–
V-CS-19_2	AD 472	skarn	9.6	–	–
V-CS-$20_{w.r.}$	AD 472	skarn	–	−1.3	17.8
V-CS-$22_{w.r.}$	AD 472	skarn	9.6	–	–
V-CS-$24b_{w.r.}$	AD 472	skarn	12.6	–	–
V-CS-$25_{w.r.}$	AD 472	skarn	16.3	–	–
V-CS-$26_{w.r.}$	AD 472	skarn	12.0	–	–
V-CS-$28_{w.r.}$	AD 472	skarn	9.6	–	–
V-CS-$29_{w.r.}$	AD 472	skarn	–	−1.3	17.8
V-CS-29_1	AD 472	skarn	15.3	–	–
V-CS-29_2	AD 472	skarn	16.6	–	–
V-CS-29_3	AD 472	skarn	14.9	–	–
V-CS-$30_{w.r.}$	AD 472	skarn	–	−1.2	18.1
V-CS-30_1	AD 472	skarn	14.4	–	–
V-CS-30_2	AD 472	skarn	15.6	–	–
V-CS-$32b_{w.r.}$	AD 472	skarn	13.2	–	–
V-CS-$32b_1$	AD 472	skarn	11.7	–	–
V-CS-$32b_2$	AD 472	skarn	15.5	–	–
V-M-$2a_{w.r.}$	AD 79	marble	–	0.41	23.9
V-M-$3a_{w.r.}$	AD 79	marble	–	−0.9	21.3
V-M-$5_{w.r.}$	AD 79	marble	–	−2.3	20.2
V-M-$6_{w.r.}$	AD 79	marble	–	0.6	24.9
V-M-$7e_{w.r.}$	AD 79	marble	–	−1.7	20.5
V-M-$8a_{w.r.}$	AD 79	marble	–	0.2	23.6
V-M-$12a_{w.r.}$	AD 79	marble	–	0.01	23.7
V-M-$15_{w.r.}$	AD 472	marble	–	−1.3	17.6
V-M-$18_{w.r.}$	AD 472	marble	–	1.3	31.5
Crustal xenoliths					
V-M-$21_{w.r.}$	AD 472	marble	–	−0.4	27.7
V-M-$23_{w.r.}$	AD 472	marble	–	0.9	28.4
V-M-$24a_{w.r.}$	AD 472	marble	–	−0.8	27.9
V-M-$32a_{w.r.}$	AD 472	marble	–	−0.7	20.8

All values reported in ‰ relative to SMOW and PDB. Analytical error is given in the text. w.r.: whole-rock; 1, 2, etc: whole-rock oxygen isotope values for skarn layers; "-": not determined.

Calculated magma $\delta^{18}O$ values from these garnets range from 8.2–9.9‰, assuming that $\Delta_{garnet\text{-}melt}$ equals $\Delta_{zircon\text{-}melt} = 1.4‰$ since, $\Delta^{18}O_{zircon\text{-}garnet} = 0‰$ (Zheng, 1993; Valley et al., 2003; Bindeman et al., 2006; Lackey et al., 2006). This implies that our whole-rock $\delta^{18}O$ values from pumice and plutonic xenolith samples are consistent with previous mineral and rock $\delta^{18}O$ values reported for Vesuvian magmatic compositions (e.g., 7.3–11.4‰, Ayuso et al., 1998; Scheibner et al., 2007).

The skarn xenoliths and corresponding skarn layers show a yet broader spectrum in oxygen isotope ratios (9.5–21.5‰), and span almost the full range between local carbonate wall-rock and Vesuvius magmatic compositions (cf. Ayuso et al., 1998) (Fig. 5a). The $\delta^{13}C$ values of calcites from the skarn xenoliths range between −4.5 and −1.2‰. The marble xenoliths, in turn, display $\delta^{13}C$ values from −2.3 to +1.3‰, with associated $\delta^{18}O$ values that range from 17.6–31.5‰ (Fig. 5b). The marble xenoliths therefore show a considerable overlap with the local unmetamorphosed marine sedimentary limestones and dolostones of the Campanian region ($\delta^{13}C$ ~1 to 3‰ and $\delta^{18}O$ >29‰; see e.g., Gilg et al., 2001 and references therein).

6. Discussion

6.1. Record of igneous processes

Previous investigations on volcanic rocks from Vesuvius have identified a number of processes operating within the magmatic system, including magma mixing, fractional crystallisation (e.g., Civetta et al., 1991; Cioni et al., 1995; Di Renzo et al., 2007), crustal assimilation (e.g., Piochi et al., 2006; Di Renzo et al., 2007; Dallai et al., 2011; Pichavant et al., 2014), and the influence of a variably metasomatised mantle source (Marianelli et al., 1995; Peccerillo, 1999, 2001; Paone, 2006).

In the following discussion, we will assess the application of binary mixing, bulk-rock assimilation (i.e., direct ingestion of carbonate rocks), and reactive wall-rock assimilation (i.e., progressive chemical and thermal interaction between magma and wall-rock) as possible explanations for the chemical variations in the presented igneous and skarn samples. Firstly, however, it is necessary to assess if the influence of secondary processes (e.g., weathering or hydrothermal alteration) can be excluded. The H_2O content of the igneous samples can be used to assess the likelihood of low-temperature alteration processes because these tend to cause simultaneous enrichment of H_2O and $\delta^{18}O$ (Table 1; e.g., Bindeman, 2008; Donoghue et al., 2008). Although our igneous samples have significantly higher $\delta^{18}O$ values than expected for regular mantle ($\delta^{18}O = 5.7 \pm 0.3‰$; Ito et al., 1987; Harmon and Hoefs, 1995; Figs. 6 and 7), water contents are generally low for all of our igneous samples (≤ 1.5 wt.%; Table 1). Therefore, our data reflect magmatic values. In this context, the pumice samples represent the magmas that resided in shallow and chemically evolving magma chamber(s) prior to eruption (Civetta et al., 1991) and the high-$\delta^{18}O$ values of Vesuvian pumices were previously considered to be the result of crustal assimilation (either in the source or at shallow depth), rather than being caused by alteration (see, e.g., Ayuso et al., 1998). The syenites, in turn, have been suggested to represent the magmatic front of

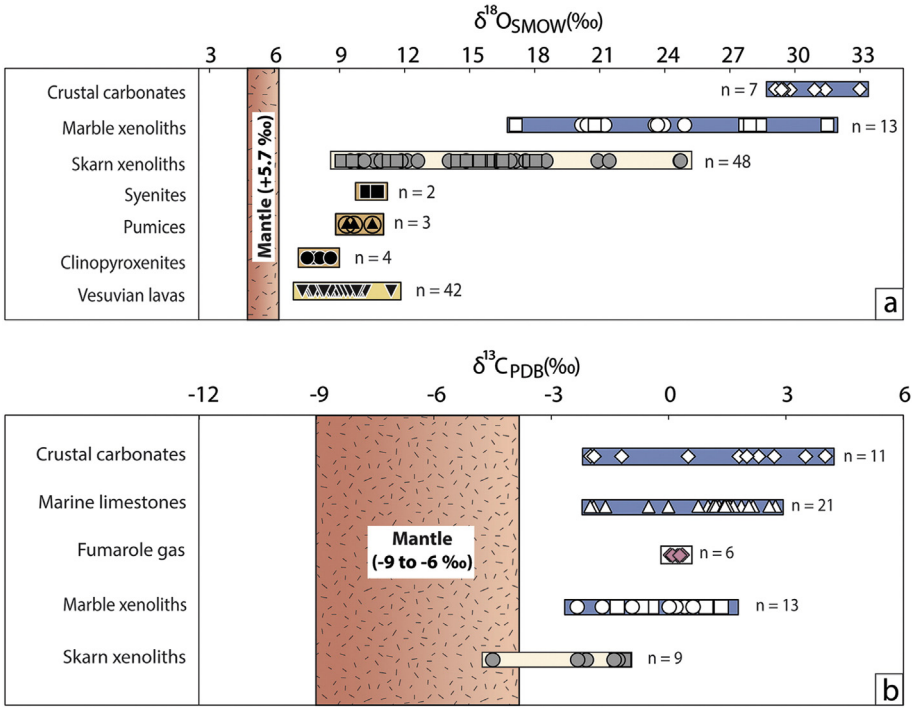

Fig. 5. a) The $\delta^{18}O$ values of igneous rocks (pumice, syenite, and clinopyroxenite) and crustal xenoliths (marbles and skarns), including skarn layers, are shown relative to mantle values. The Vesuvian lava field (n = 42) and crustal carbonate field from the Campanian region (n = 7) are constructed after Ito et al. (1987); Eiler et al. (1996); Ayuso et al. (1998); Gilg et al. (2001); Del Moro et al. (2001); Fulignati et al. (2005a). Note the range of $\delta^{18}O$ in the skarn xenoliths spans from the igneous samples towards the crustal carbonates. b) Range of $\delta^{13}C$ for the Vesuvius skarn and marble xenolith samples in comparison with reference fields for mantle, local carbonate from the Campanian region (n = 11), marine carbonate (n = 21) and Vesuvius fumarole gases (n = 6) (Symbols as in Fig. 3 and data source for reference fields from Weber and Woodhead, 1969; Javoy et al., 1986; Taylor, 1986; Sano and Marty, 1995; Hoefs, 1996; Allard et al., 1997; Tedesco, 1997; Chiodini et al., 2001; Hilton et al., 2002; Parente et al., 2007; Iacono-Marziano et al., 2009).

the outermost parts of the Vesuvius magma reservoir system with dominantly mantle-derived compositions based on Sr-Nd-Pb isotope compositions (De Vivo et al., 1995). High $\delta^{18}O$ values of these samples (10.3–10.8‰) have, in contrast, been interpreted by others to represent interaction of Vesuvius magma with the carbonate rocks of the chamber roof (Fulignati et al., 2001, 2004). Finally, the Cr-rich clinopyroxenite xenoliths have been considered to result from crystal accumulation in the lower portions of the Pompeii and Pollena chambers (Hermes and Cornell, 1981; Cioni et al., 1995; Fulignati et al., 2001, 2004), while Cr-poor clinopyroxenites are regarded as portions of a peripheral crystallisation zone near in the lower part of the magma reservoir (e.g., Belkin et al., 1985; Fulignati et al., 2001, 2004). These textural interpretations, coupled with high $\delta^{18}O$ but low H_2O observed in all igneous samples, imply that considerably portions of the Vesuvius volcanic system are affected by magma–crust interaction. This notion is consistent with a recent oxygen isotope study on Vesuvius olivine and clinopyroxene in shoshonite to tephrite compositions that revealed relatively primitive samples were already contaminated by carbonate-derived CO_2 during early stages of crystallisation in the crust (Dallai et al., 2011). Indeed, the $\delta^{18}O$ values of olivine reported from Vesuvius range between 5.5 and 7.1‰ (Dallai et al., 2011) and are thus significantly higher than the typical $\delta^{18}O$ values of mantle derived-olivine (5.2 ± 0.3‰; Mattey et al., 1994).

In order to quantify the relative roles of assimilation processes in our sample suite, we have modelled the effects of crustal additions using binary mixing and combined assimilation and fractional crystallisation, AFC (De Paolo, 1981) and energy-constrained AFC (EC-AFC; Spera and Bohrson, 2001). The three models gave similar results and we only discuss the EC-AFC model herein. The binary mixing and traditional AFC modelling is provided in Supplementary Material 2.

We have produced two different EC-AFC simulations. The first one considers a parental magma representative of a primitive Vesuvius composition, while the second one uses an evolved Vesuvius magma. In both models, magmas are contaminated by carbonate crust, the dominant crustal lithology that was encasing the Pompeii and Pollena magma reservoir (cf. Scaillet et al., 2008). In our simulations, the initial melt temperature was assumed to be 1200 °C, similar to that obtained from data of melt inclusions (Marianelli et al., 1995). A temperature of 700 °C (T_a^0) was assigned for the direct Vesuvius carbonate basement (Pappalardo et al., 2004). The liquidus temperature (T_{la}) and the solidus temperature (T_s) of carbonate wall-rock are taken to be 1000 °C and 800 °C, respectively (see Lentz, 1999; Wenzel et al., 2002). The model requires the definition of the equilibration temperature (T_{eq}), which describes the approach of the system to equilibrium during the processes of heat exchange. This temperature is equal to or higher than eruptive temperature (Spera and Bohrson, 2001). Here, we chose an equilibrium temperature of 950 °C (e.g., Cioni et al., 1998; Marianelli et al., 1995; Dallai et al., 2011). Crystallisation and fusion enthalpies and isobaric specific heats and non-linear logistical parameters have been set to default values, as recommended by Spera and Bohrson (2001). In the modelling, Sr in the carbonate assimilant is assumed incompatible to compatible (bulk $D_0 = 0.1$ to 1; e.g., Barnes et al., 2005), and compatible in the magmas (bulk $D_0 = 1$; e.g., Pappalardo et al., 2004). For Zr, the distribution coefficients of magma and carbonate assimilant have been considered identical (bulk $D_0 = 0.2$ to 0.4; Mantovani and Hawkesworth, 1990; Pappalardo et al., 2004; Di Renzo et al., 2007). Further details on the end-member compositions are given in Section 2.2 and the modelling parameters are reported in Table 4.

The models reproduce the differentiation sequence in terms of $\delta^{18}O$, Sr and Zr values (Fig. 6a-b). Clinopyroxenites, for example, record high $\delta^{18}O$ values of ~8.0‰ (average $\delta^{18}O$) relative to typical mantle values most probably due to limited interaction with carbonate wall-rocks. Pumices, in turn, evolved towards more differentiated compositions while progressively interacting with the local carbonates, causing elevated $\delta^{18}O$ values up 10.5‰. The EC-AFC simulations imply that at least two types of parental magma are required to explain the

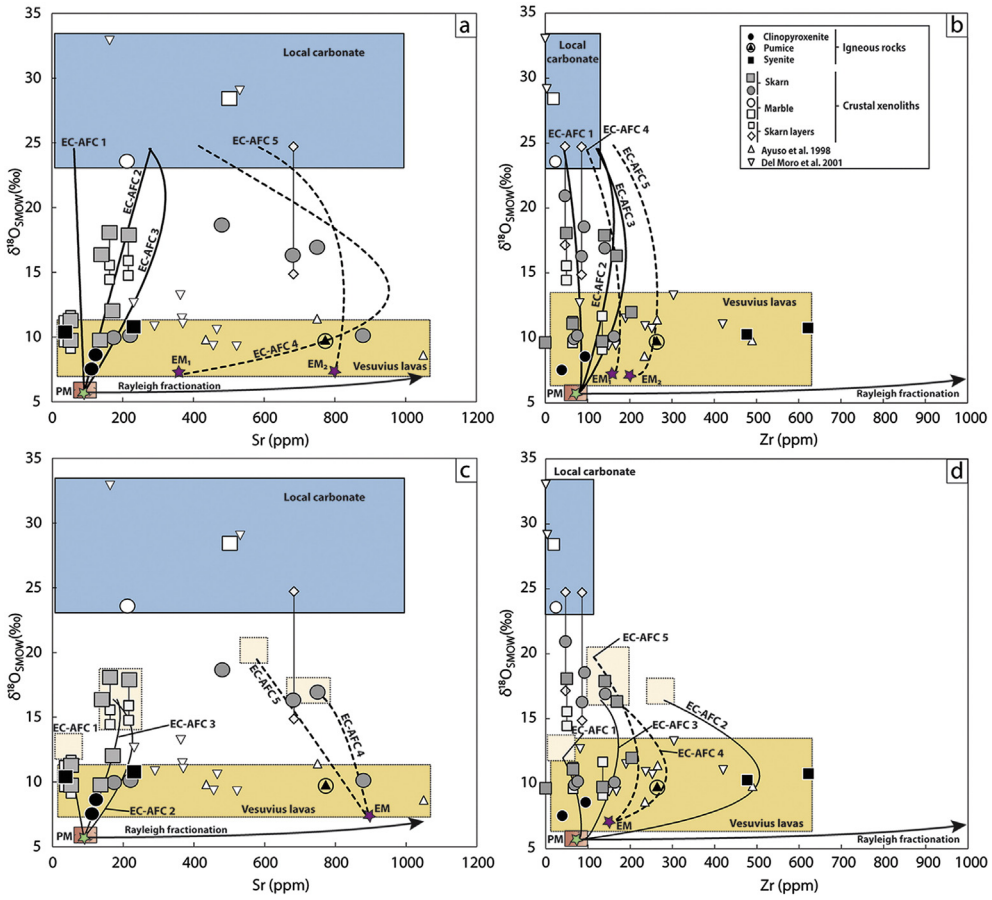

Fig. 6. Oxygen isotope vs Sr and Zr results from EC-AFC modelling (after Bohrson and Spera, 2001; Spera and Bohrson, 2001). Modelling results are indicated by black solid and dashed lines and are calculated on the basis of the parameters listed in Table 4. The fields of primitive parental magmas (red box), common Vesuvian lavas (orange box), and local carbonate crust (blue box) are given for comparison. Analytical uncertainties are smaller than symbol size. The symbols connected by tie lines are skarn layers from individual samples. The Rayleigh fractionation trend (flat-lying black arrow) illustrates the changes in $\delta^{18}O$ values expected from closed-system fractional crystallisation (after Taylor and Sheppard, 1986; Bindeman et al., 2005; Bindeman, 2008). The evolutionary paths EC-AFC 1 to 3 (solid lines) use a primitive parental magma composition (PM; green star) while EC-AFC 4 and 5 (dashed lines) employ an evolved Vesuvius magma (EM; purple stars). Direct magma–carbonate interaction (limestone or dolostone) can reproduce most of the geochemical variations of the AD 79 and AD 472 igneous rocks and skarn xenoliths (a & b). However, to explain the full range of $\delta^{18}O$ values of the Vesuvius magma compositions, interaction with variable skarn compositions is also required (cream-coloured boxes in c & d). See text for details. Symbols as in Fig. 3 and data sources as in Fig. 5a and from Ito et al. (1987); Eiler et al. (1996); Ayuso et al. (1998); Gilg et al. (2001); Del Moro et al. (2001); Fulignati et al. (2005a); Parente et al. (2007); Iacono-Marziano et al. (2009).

geochemical variations displayed by the analysed samples, a primitive one and a differentiated one. This is because the range of $\delta^{18}O$ values detected in the igneous rocks cannot be explained by closed system Rayleigh-style fractionation, which would only allow for an increase in $\delta^{18}O$ of ≤1‰ (see also calculated curve in Fig. 6a-b; e.g., Taylor and Sheppard, 1986; Bindeman et al., 2005; Bindeman, 2008). In this context, the magma storage system for the AD 79 event has been characterised as a large and 'mature' magma reservoir that was emplaced at ~7 to 8 km depth, and was refilled with new magma batches in a frequency of ~10^3 years (Fulignati et al., 2004; Morgan et al., 2006; Scaillet et al., 2008). In contrast, the AD 472 magma reservoir was more of the 'evolving' type and was residing at shallower levels of ~3 to 4 km depth. Frequent injection of small mafic magma batches (cf. Scaillet et al., 2008) may have continuously renewed reaction surfaces and promoted more or less direct magma–carbonate interaction (cf. Pichavant et al., 2014). Hence the major and trace element variations observed in our rock samples from the Pompeii and Pollena eruptions reflect in part also interaction processes at slightly different crystallisation levels and differences in magma supply to these distinct levels (cf. Fulignati et al., 2004; Freda et al., 2008; Pichavant et al., 2014). The exact type of crustal carbonate that affected the igneous compositions (limestone or dolostone) likely also played a role, but is difficult to assess with O and C isotopes only due to the broad isotopic range of the local crustal carbonates (see, e.g., Civetta et al., 1991; Del Moro et al., 2001; Fulignati et al., 2004; Piochi et al., 2006; Iannace et al., 2011). Mineral assemblages, and MgO and Sr contents in our sample suite, however, provide some insights into the nature of the variability of carbonate assimilated during the Pollena and the Pompeii eruptions. For example, while almost all Pollena skarns show high MgO and low-Sr content with olivine and calcite in the mineral assemblage, most of the Pompeii skarns exhibit low MgO and high-Sr content, and calcite as the main mineral phase. This implies that the assimilated carbonate during the AD 79 event was more limestone dominated, while the contaminants that affected the AD 472 magmas had a higher dolostone component (Figs. 3, 4 and 6).

6.2. Skarn formation during magma–carbonate interaction

The geochemical variability amongst the skarn xenoliths is likely the result of variety of processes, including thermal (pyro-) metamorphism, infiltration metasomatism, and direct reaction between magma and carbonate at the contact with a magmatic body (cf. Meinert, 1992). To quantitatively assess the inter-relationship between our skarn samples, we now discuss oxygen and carbon isotopes as tracers of fluid sources and fluid-rock interaction (e.g., Taylor and Bucher-Nurminen, 1986; Bowman, 1998). Vesuvian skarn xenoliths display $\delta^{18}O$ and $\delta^{13}C$ values that are considerably lower than those of the carbonate wall-rock (Fig. 7; Ayuso et al., 1998; Gilg et al., 2001; Del Moro et al., 2001;

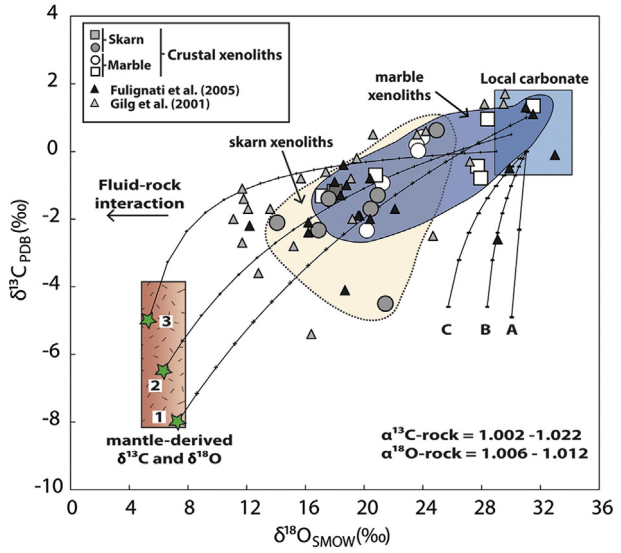

Fig. 7. Plot of $\delta^{13}C$ vs. $\delta^{18}O$ for calcites from marbles (white) and skarn xenoliths (grey), including complementary data by Fulignati et al. (2005a) and Gilg et al. (2001). Analytical uncertainties are smaller than symbol size. Lines A, B, and C are trends for pure Rayleigh decarbonation, starting with unmetamorphosed crustal carbonate. Fractionation factors used for the decarbonation model are indicated (after Valley, 1986). Lines 1, 2 and, 3 are mixing trends at 5% intervals between a crustal carbonate ($\delta^{13}C = +0.5‰$; $\delta^{18}O = +31‰$) and a mantle-type magmatic composition ($\delta^{13}C = -4$ to $-8‰$; $\delta^{18}O = +5.3$ to $+7.3‰$; Taylor, 1986; Valley, 1986).

Fulignati et al., 2005a). Trajectories A, B, and C in Fig. 7 represent the effects of Rayleigh de-volatilisation of a crustal carbonate at >500 °C (Valley, 1986). The equilibrium de-carbonation reaction, i.e., pure thermal carbonate breakdown (or the so-called 'calc-silicate limit') assumes that if reaction goes to completion, all carbon in the carbonate is released as CO_2 while only ~40% of oxygen is lost (Valley, 1986). Marbles with high $\delta^{18}O$ values (≥ 28‰; n = 4), but slightly lower $\delta^{13}C$ values relative to the carbonate protolith(s), are consistent with dominantly thermal carbonate break-down, but require some exchange between fluid and rock, or mixing with internal non-carbonate fluids (cf. Nabelek et al., 1984; Melezhik et al., 2003). The $\delta^{18}O$ and $\delta^{13}C$ values measured in some of the marbles and in virtually all of the skarn xenoliths do, however, plot away from the pure decarbonation curves (A to C), implying that the large isotopic shifts observed cannot be produced by decarbonation reactions alone. Indeed, $\delta^{18}O$ and $\delta^{13}C$ values of these samples tend to follow binary mixing trajectories between magma and carbonate wall-rock (1, 2, and 3 in Fig. 7). This reflects that depletion of oxygen and carbon isotope compositions from marble to skarn can be attributed to CO_2 release on progressive skarn formation due to magma–carbonate interaction (cf. Taylor and O'Neil, 1977; Bowman et al., 1985; Valley, 1986; Orhan et al., 2011).

The quantitative models of magma–carbonate interaction in Fig. 6a-b can further help to explain the geochemical variations observed in the skarn xenoliths (see also Table 4 and Supplementary Material 2). For example, curves EC-AFC 1 to 3 are consistent with an initial stage of reaction. A relatively primitive Vesuvius magma composition is emplaced into carbonate substrata and direct magma–carbonate interaction produces the high $\delta^{18}O$ in some skarns, e.g., those from the AD 472 eruption. Subsequently, the primitive Vesuvius magma may differentiate by, e.g., AFC-type processes, that include a closed-system fractional crystallisation component of ≤1‰ in $\delta^{18}O$, to a typical Vesuvian phono-tephritic/tephriphonolitic composition. This combined assimilation coupled with fractionation can explain the high $\delta^{18}O$ in other skarn xenoliths, e.g., some of the AD 79 skarns (curves EC-AFC 4 and 5; Fig. 6a–b). Moreover, the broad range in $\delta^{18}O$ values of the skarn xenoliths, which spans from values similar to the host magmas to values akin to those of the marble xenoliths, implies that skarn xenoliths with low $\delta^{18}O$ values most probably experienced longer or more intense interaction with the host magma(s) and hence inherited a more typical "igneous signature". In turn, xenoliths with high $\delta^{18}O$ values (i.e., those more similar to the carbonates) likely had a shorter interaction times or originate from the outer contact aureole (Fig. 6a–b). The nature of the protolith from where the skarns have originated is more difficult to distinguish using $\delta^{18}O$ or $\delta^{13}C$ ratios, but usually high MgO content of some skarns is associated with low-Sr, while low MgO is often coupled with high-Sr in our skarn samples. In the context of this study, high-Sr skarns are likely representative of former limestone on our plots, while low-Sr skarns are more characteristic for former limestone compositions. This suggests that the original protoliths (dolostone or limestone) are still traceable through some components (see also Section 6.1 above).

Table 4
Parameters of EC-AFC model.

Equilibration parameters			
Liquidus temperature, $T_{l,m}$	1200 °C	Crystallisation enthalpy, Δh_m (Jkg^{-1})	396,000
Initial temperature, T^0_m	1200 °C	Isobaric specific heat of magma, $C_{p,m}$ ($Jkg^{-1}K^{-1}$)	1484
Liquidus temperature, T_{la}	1000 °C	Fusion enthalpy, Δh_a (Jkg^{-1})	250,000
Initial temperature, T^0_a	700 °C	Isobaric specific heat of assimilant, $C_{p,a}$ ($Jkg^{-1}K^{-1}$)	1300
Solidus temperature, T_s	800 °C		
Equilibration temperature, T_{eq}	950 °C		

	EC-AFC 1	EC-AFC 2	EC-AFC 3	EC-AFC 4	EC-AFC 5
Magma–carbonate interaction modelling					
Magma					
Sr (ppm)	90	90	90	350	800
Bulk D_0	1	1	1	1	1
Zr (ppm)	75	75	75	150	200
Bulk D_0	0.4	0.4	0.4	0.4	0.1
$^{87}Sr/^{86}Sr$	0.7066	0.7066	0.7066	0.7077	0.7077
$\delta^{18}O$ (‰)	5.7	5.7	5.7	7	7
Assimilant					
Sr (ppm)	50	350	350	600	500
Bulk D_0	1	1	0.5	0.1	0.5
Zr (ppm)	4.9	100	100	20	23
Bulk D_0	0.4	0.4	0.2	0.2	0.2
$^{87}Sr/^{86}Sr$	0.709	0.709	0.709	0.709	0.709
$\delta^{18}O$ (‰)	31.0	31.0	31.0	31.0	31.0
Magma-xenolith interaction modelling					
Magma					
Sr (ppm)	90	90	90	900	90
Bulk D_0	1	1	1	1	1
Zr (ppm)	75	90	90	150	150
Bulk D_0	0.4	0.4	0.4	0.4	0.4
$^{87}Sr/^{86}Sr$	0.7066	0.7066	0.7066	0.7077	0.7077
$\delta^{18}O$ (‰)	5.7	5.7	5.7	7	7
Assimilant					
Sr (ppm)	33	216	216	700	450
Bulk D_0	1	0.4	0.7	0.9	1
Zr (ppm)	4.9	304	100	100	50
Bulk D_0	0.2	0.1	0.4	0.1	0.1
$^{87}Sr/^{86}Sr$	0.7074	0.7074	0.7074	0.7074	0.7074
$\delta^{18}O$ (‰)	14	20	20	20	24

Magma and assimilant initial and solidus and liquidus temperatures are after literature constraints (Marianelli et al., 1995; Pappalardo et al., 2004; Lentz, 1999; Wenzel et al., 2001, Wenzel et al., 2002). Crystallisation and fusion enthalpies and isobaric specific heats and non-linear logistical parameters are taken from Spera and Bohrson (2001). End-members compositional ranges: *i*) Parental magma: Ito et al. (1987); Eiler et al. (1996); Wilson (1997); *ii*) Evolved magma and carbonate: Ayuso et al. (1998); D'Antonio et al. (1999); Del Moro et al. (2001); Civetta et al. (2004); Di Renzo et al. (2007) and this study; *iii*) Calc-silicates: Del Moro et al. (2001); Gilg et al. (2001) and this study.

6.3. Skarn recycling

Magmas emplaced into a carbonate crust form a thermo-metamorphic and/or metasomatic aureole. A marble aureole develops during early stages of contact metamorphism, and then skarn rocks form (e.g., Rittmann, 1962; Meinert, 1992; Coulson et al., 2007; Gaeta

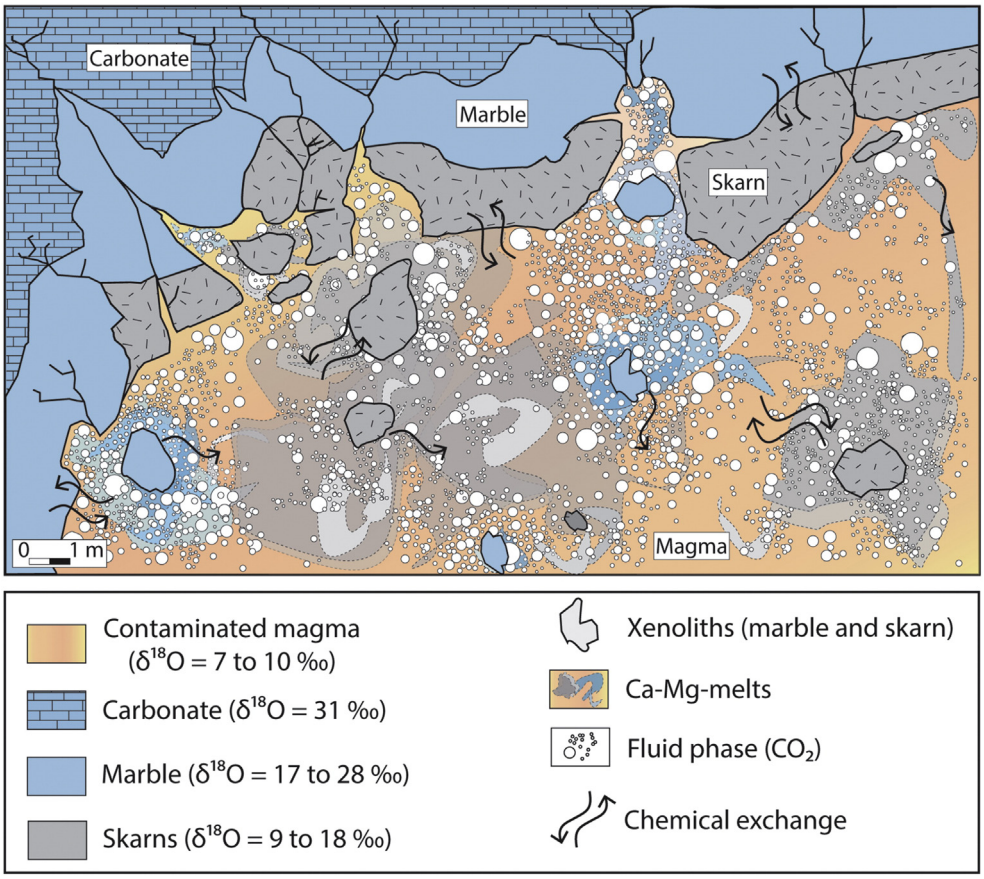

Fig. 8. Schematic diagram illustrating reaction between magma, limestone, and skarn beneath Vesuvius prior to and during, e.g., the Pompeii and Pollena eruptions. Conversion of carbonate into marble occurs during early stages of contact metamorphism. Progressive reactions between carbonate, marble, and the magma body produce skarn-rocks and liberate CO_2. With time, the marbles and skarns that form in the aureole increasingly limit the assimilation of pure limestone and skarn assimilation may become dominant. Fresh reaction surfaces between magma and limestone are, however, repeatedly created during, e.g., volcano unrest and through earthquakes, tremors, magma migration, thermal cracking or dyking (e.g., Deegan et al., 2011), and thus a full range of limestone to skarn samples is preserved in the eruptive deposits (see text for details).

et al., 2009: Mollo et al., 2010). The geochemical characteristics of marble and skarn xenoliths in the studied pyroclastic sequences imply that direct magma–carbonate interaction and skarn recycling likely both acted as contamination processes (Figs. 6c–d and 8; e.g., Gaeta et al., 2009; Troll et al., 2013). During metamorphism and magma-xenolith interaction, limestone and dolostone react to marble and skarn xenoliths and produce Ca-rich or Ca-Mg-rich melt(s) through decarbonation reactions and associated mass loss- and gain between magma and contaminant (e.g., Gaeta et al., 2009; Deegan et al., 2010; Mollo et al., 2010; Di Rocco et al., 2012; Jolis et al., 2013). Such reactions are continuous and the related chemical exchange between crustal carbonate/marble and magma is reflected in the magma through a relative Si- and Al-loss, but Ca- and Mg-gain. In turn, skarns have taken up Si and Al as well as typically incompatible trace elements such as Nb, Th, Zr, but lost Ca and Mg as well as some incompatible trace elements such as Ce or Y (see also Watson et al., 1982; Meinert, 1992; Coulson et al., 2007; Dyer et al., 2011).

Using a range of calc-silicate compositions as contaminants and a spectrum of Vesuvius magma compositions with variable Sr and oxygen isotopic starting values, we modelled magma–skarn interaction to verify the chemical conditions required to explain the range of isotopic values displayed by our sample suite (Fig. 6c-d). The high $\delta^{18}O$ values of the igneous samples are consistent with assimilation of skarns into either a primitive parental magma or an already evolved Vesuvius magma. The effect of skarn assimilation into the magma is furthermore consistent with the presence of similar mineral associations in the skarns and some of the igneous samples (Table 2) and with the broad range of $\delta^{18}O$ values recorded in the skarn xenolith suite. The $\delta^{18}O$ values in particular show a link between an increasing metamorphic grade (mineralogy and lithology) and increasingly more 'igneous' isotope signature, which underlines the exchange between magma and skarn samples.

At a more advanced stage of interaction, a thick skarn aureole may temporarily inhibit direct carbonate assimilation, and may provide a physical barrier to further contamination. At that point skarn recycling may become the dominant contamination processes (Fig. 6c-d and 8).

6.4. Quantifying CO_2 liberation by magma–carbonate interaction

Decarbonation of crustal carbonate in contact with magma will reduce CO_3 in the affected crustal rock by liberation of CO_2 and uptake of SiO_2 (e.g., Rittmann, 1962; Behrens et al., 2009; Gaeta et al., 2009; Ganino et al., 2008; Ganino and Arndt, 2009; Troll et al., 2012; Heap et al., 2013). The liberated CO_2, in turn, will contribute to a volcano's gas budget (e.g., Freda et al., 1997, 2011; Iacono-Marziano et al., 2009; Goff et al., 2001; Ganino and Arndt, 2009; Mollo et al., 2010, 2012; Troll et al., 2012; Troll et al., 2013). Indeed, the $\delta^{13}C$ values of present day Vesuvius fumarole gases are characteristic of marine carbonate rocks ($\delta^{13}C = -2$ to $+4$‰; Parente et al., 2007; Iacono-Marziano et al., 2009), pointing to a considerable fraction of non-magmatic CO_2 that is currently liberated at Vesuvius. Given that carbonate dissolution by juvenile Vesuvius magma is likely rapid (e.g., Jolis et al., 2013), considerable amounts of 'extra' CO_2 may have been liberated before and during the Pompeii and Pollena explosive events in addition to the volatile components provided by the magmas (cf. Deegan et al., 2011). To quantify the potential amount of CO_2 produced by contact

Table 5
Magma reservoir and associated contact aureole volume for different reservoir geometries (i.e., 5, 10, 20, 30% addition to the axis of the magma reservoir), and conversion efficiencies (50–100%) to yield magmatic CO_2 versus non-magmatic CO_2 (in %) and associated factors.

Magma chamber volume (km^3)	Magmatic CO_2 (Gt)	Aureole volume (km^3) [5%]	Carbonate efficiency (Gt)					
			50%	60%	70%	80%	90%	100%
			Non-magmatic CO_2 factors					
			7	8	10	11	12	14
			Non-magmatic CO_2 (Gt)					
0.01	0.0001	0.002	0.001	0.001	0.001	0.002	0.002	0.002
0.5	0.01	0.08	0.05	0.06	0.07	0.08	0.09	0.1
1	0.01	0.16	0.10	0.11	0.13	0.15	0.17	0.19
5	0.07	0.79	0.48	0.57	0.67	0.76	0.86	0.95
10	0.14	1.58	0.95	1.14	1.33	1.52	1.71	1.90
50	0.69	7.88	4.76	5.71	6.66	7.61	8.56	9.52
75	1.03	11.82	7.14	8.56	9.99	11.42	12.85	14.27
100	1.38	15.76	9.52	11.42	13.32	15.22	17.13	19.03
200	2.75	31.53	19.03	22.84	26.64	30.45	34.25	38.06
300	4.13	47.29	28.54	34.25	39.96	45.67	51.38	57.09
400	5.50	63.05	38.06	45.67	53.28	60.89	68.51	76.12
500	6.88	78.81	47.57	57.09	66.60	76.12	85.63	95.15
Magma chamber volume (km^3)	Magmatic CO_2 (Gt)	Aureole volume (km^3) [10%]	Carbonate efficiency (Gt)					
			50%	60%	70%	80%	90%	100%
			Non-magmatic CO_2 factors					
			15	17	20	23	25	29
			Non-magmatic CO_2 (Gt)					
0.01	0.0001	0.003	0.002	0.0024	0.0028	0.0032	0.0036	0.0040
0.5	0.007	0.17	0.10	0.12	0.14	0.16	0.18	0.20
1	0.014	0.33	0.20	0.24	0.28	0.32	0.36	0.40
5	0.07	1.66	0.99	1.20	1.40	1.60	1.80	2.00
10	0.14	3.31	1.99	2.40	2.80	3.20	3.60	4.00
50	0.69	16.55	9.99	12.00	13.99	15.98	17.98	19.98
75	1.03	24.83	14.98	17.98	20.98	23.98	26.97	29.97
100	1.38	33.10	19.98	23.98	27.97	31.97	35.96	39.96
200	2.75	66.20	39.96	47.95	55.94	63.94	71.93	79.92
300	4.13	99.30	59.94	71.93	83.91	95.90	107.89	119.88
400	5.50	132.40	79.92	95.90	111.89	127.87	143.86	159.84
500	6.88	165.50	99.90	119.88	139.86	159.84	179.82	199.80
Magma chamber volume (km^3)	Magmatic CO_2 (Gt)	Aureole volume (km^3) [20%]	Carbonate efficiency (Gt)					
			50%	60%	70%	80%	90%	100%
			Non-magmatic CO_2 factors					
			32	38	45	51	58	64
			Non-magmatic CO_2 (Gt)					
0.01	0.0001	0.007	0.004	0.005	0.006	0.007	0.008	0.009
0.5	0.007	0.36	0.22	0.26	0.31	0.35	0.40	0.44
1	0.01	0.73	0.44	0.53	0.62	0.70	0.79	0.88
5	0.07	3.64	2.20	2.64	3.08	3.52	3.96	4.39
10	0.14	7.28	4.39	5.27	6.15	7.03	7.91	8.79
50	0.69	36.40	21.97	26.37	30.76	35.16	39.55	43.94
75	1.03	54.60	32.96	39.55	46.14	52.73	59.32	65.92
100	1.38	72.80	43.94	52.73	61.52	70.31	79.10	87.89
200	2.75	145.60	87.89	105.47	123.04	140.62	158.20	175.78
300	4.13	218.40	131.83	158.20	184.56	210.93	237.30	263.66
400	5.50	291.20	175.78	210.93	246.09	281.24	316.40	351.55
500	6.88	364.00	219.72	263.66	307.61	351.55	395.50	439.44
Magma chamber volume (km^3)	Magmatic CO_2 (Gt)	Aureole volume (km^3) [30%]	Carbonate efficiency (Gt)					
			50%	60%	70%	80%	90%	100%
			Non-magmatic CO_2 factors					
			53	63	74	84	95	105
			Non-magmatic CO_2 (Gt)					
0.01	0.0001	0.01	0.007	0.009	0.010	0.012	0.01	0.014
0.5	0.007	0.60	0.36	0.43	0.51	0.58	0.65	0.72
1	0.01	1.20	0.72	0.87	1.01	1.16	1.30	1.45
5	0.07	5.99	3.61	4.34	5.06	5.78	6.50	7.23
10	0.14	11.97	7.23	8.67	10.12	11.56	13.01	14.45
50	0.69	59.85	36.13	43.35	50.58	57.80	65.03	72.25

Table 5 (*continued*)

Magma chamber volume (km^3)	Magmatic CO_2 (Gt)	Aureole volume (km^3) [30%]	Carbonate efficiency (Gt)					
			50%	60%	70%	80%	90%	100%
			Non-magmatic CO_2 factors					
			53	63	74	84	95	105
			Non-magmatic CO_2 (Gt)					
75	1.03	89.78	54.19	65.03	75.87	86.71	97.54	108.38
100	1.38	119.70	72.25	86.71	101.16	115.61	130.06	144.51
200	2.75	239.40	144.51	173.41	202.31	231.21	260.11	289.02
300	4.13	359.10	216.76	260.11	303.47	346.82	390.17	433.52
400	5.50	478.80	289.02	346.82	404.62	462.43	520.23	578.03
500	6.88	598.50	361.27	433.52	505.78	578.03	650.29	722.54

metamorphic process relative to the magmatic volatile fraction for the two eruptions in question, we first evaluate the magnitude of magmatic CO_2 that could have been released, followed by an evaluation of the CO_2 contribution from the metamorphic aureoles to the two respective magma reservoirs.

Volatile contents in melt inclusions provide information on pre-eruptive, i.e., the original CO_2 and H_2O contents of the parental magma (e.g., Wallace, 2005). Studies of the Pompeii and Pollena melt inclusions indicate that phonolite and tephriphonolite magmas were H_2O and CO_2 vapour dominated (e.g., Belkin et al., 1998; Marianelli

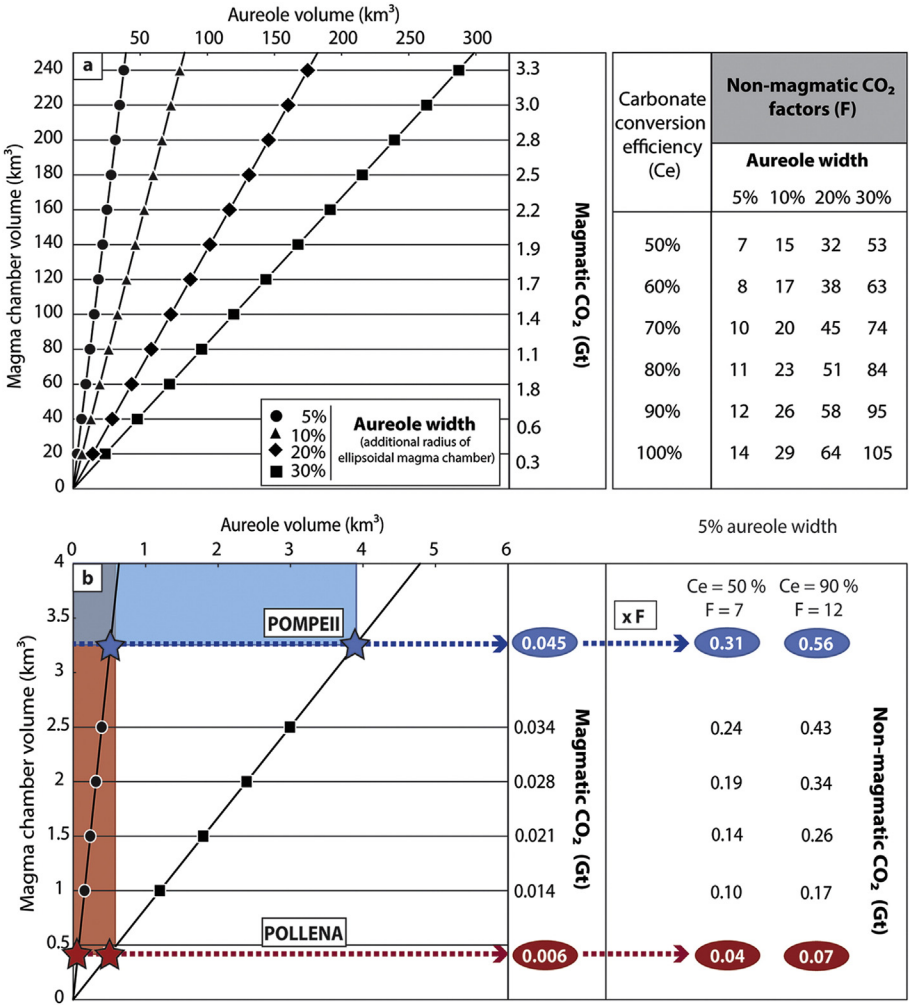

Fig. 9. (a) Diagram showing relationships for different magma reservoir and aureole volumes, ranging from <1 to ~240 km^3 (see also Table 5). Average expected magmatic CO_2 is given on the right hand y-axis (after Self et al., 2006). The magma chamber ellipsoid is considered to be surrounded by an aureole shell thickness of 5 to 30% of additional length of the ellipsoid axes. (b) The non-magmatic CO_2 can be computed using the expression $M_{C.A.CO_2} = F \times M_{ECO_2}$, where $M_{C.A.CO_2}$ is the mass of CO_2 released by contact metamorphism (in kg), M_{ECO_2} is the mass of magmatic CO_2 released (in kg), and F is a conversion factor related to aureole width and carbonate conversion efficiency (Ce; set between 50% and 100%; see also Table 5 and Supplementary Material 3). Example calculation for the Pompeii (blue star) and Pollena (red star) eruptions assume an aureole width of 5% added axis length and an efficiency of carbonate conversion of between 50 to 90%. The dashed blue and red lines connect the Pompeii and Pollena eruptions with (*i*) aureole volume, (*ii*) potential magmatic CO_2 contribution, and (*iii*) the potential non-magmatic CO_2 contributions from the aureole. The resulting non-magmatic CO_2 contributions is then between factors 7 and 12 higher than the magmatic one (for 50 to 90% carbonate conversion efficiency, respectively), consistent with estimates for intrusions into volatile-rich sedimentary strata elsewhere (Ganino et al., 2008; Ganino and Arndt, 2009; Aarnes et al., 2010, 2011a, 2011b).

et al., 1999; Cioni, 2000; Webster et al., 2003; Fulignati et al., 2005b; Fulignati and Marianelli, 2007; Balcone-Boissard et al., 2012). However, the melt inclusions also record strong degassing during repeated injections, which implies that at least a fraction of the magmatic CO_2 was already released before (shallow) entrapment of the melt inclusions (Fulignati et al., 2005b; Cioni, 2000; Fulignati and Marianelli, 2007; Balcone-Boissard et al., 2012). Exact quantities of pure magmatic CO_2 contributions are thus difficult to estimate from melt inclusion data alone.

To provide a first order assessment of the proportions of magmatic CO_2 relative to crustal CO_2 from contact aureoles for the investigated eruptive events, and to present an application for other volcanic systems where shallow-magma chambers are emplaced into carbonate-rich rocks, we have integrated the approaches and associated formulations of Self et al. (2006) and Ganino et al. (2008) (Table 5). Although magma chambers can vary in shapes and size (cf. Barnes et al., 2009), we consider the eruptive volume of a unit as the minimum magma reservoir volume contained in an ellipsoidal reservoir with two of the semi-axes of equal (longer) length. Then, from this calculated magma reservoir volume, estimates of the aureole size are made by fractional additions to the three axis of the ellipsoidal magma reservoir, thus defining a variably thick 'aureole shell'. Metamorphic aureoles to magma reservoirs show thicknesses of between 30% and 200% of the intrusion thickness or diameter, which depends on (*i*) the composition and original temperature of the host rock, (*ii*) the temperature of the magma body, and (*iii*) the temporal evolution of the intrusion or pluton (Aarnes et al., 2010, 2011a, 2011b; Svensen and Jamtveit, 2010). Lacking detailed information on geometry and structure of metamorphic aureoles at depth beneath Vesuvius, we consider a conservative range of aureole shell thicknesses from between 5% and 30% added to the axes length of the ellipsoidal magma reservoir (cf. Aarnes et al., 2010), thus providing a first order approximation for our considerations (see Table 5 and Supplementary Material 3 for details).

To quantify the mass of magmatic CO_2 released, we assume that magma undergoes 100% degassing. Using the erupted volumes, a mass fraction of 0.005 of CO_2 in the melt, and a rock density of 2750 kg m^{-3} (Self et al., 2006; see Fig. 9 and Supplementary Material 3), a first order estimate of magmatic CO_2 released can be achieved. Note, however, that any eruptive material will retain a small percentage of CO_2 in the erupted products (e.g., Wallace, 2005), making this estimate likely a little too high. In turn, non-erupted magma may also have contributed some CO_2, but we are not in a position to account for this aspect in this simplified approach.

To approximate the CO_2 potentially released due to contact-metamorphism, we then consider the mass of CO_2 released from an aureole shell. We use these relationships to define a calculation factor for 'non-magmatic CO_2' relative to magmatic CO_2, so that it can be applied to variable chamber volumes (see Table 5 and Supplementary Material 3). The non-magmatic CO_2 is derived by using (*i*) the CO_2 liberated from 1 kg of limestone (439 g of CO_2 for complete decarbonation; Deer et al., 1992), (*ii*) the contact aureole volume, and (*iii*) the rock density of 2750 kg m^{-3} (e.g., Ganino et al., 2008) (see also Table 5 and Fig. 9 for further examples, and Supplementary Material 3 for detailed explanation).

Applying this approach to the Pompeii and Pollena eruptions allows us to approximate the combined amount of CO_2 released during these events. Employing 3.25 and 0.42 km^3 of eruptive products for the Pompeii and Pollena events, respectively (DRE; Cioni et al., 2008), 0.045 Gt and 0.006 Gt of magmatic CO_2 are calculated. If we consider a minimum value of 5% extra axis length of a broadly ellipsoidal reservoir as the aureole shell volume and an efficiency range of between 50 and 90% for the decarbonation reaction in the aureole, then the amount of CO_2 liberated from such a 'thin' contact aureole falls between 0.31 and 0.56 Gt of CO_2 for the Pompeii eruption and between 0.04 and 0.07 Gt for the Pollena event (Fig. 9). This equates to factors of crustal CO_2 relative to the magmatic CO_2 of between 7 and 12 for 50 to 90% conversion efficiency. The computed results compare favourably with the calculations of Ganino and Arndt (2009) for, e.g., the Panzhihua intrusion in China, where 11.2 Gt of non-magmatic CO_2 may have been liberated relative to ~2 Gt of magmatic CO_2, but notably from a CO_2-poorer mixed shale and carbonate aureole.

The present day shallow magma reservoir at Vesuvius (e.g., ~2 km high and ~10 km wide; see De Lorenzo et al., 2006 and references therein), may contain up to 105 km^3 of magma in this volume, which can produce ~1.4 Gt of magmatic CO_2. Assuming limestone-dominated aureole volume of an extra 5–30%, as above in our model calculation, the total amount of CO_2 that can potentially be emitted through contact metamorphism from such a reservoir system is then between factor 7 and 12 higher than the magmatic CO_2, and calculates to between 10 and 18 Gt (Fig. 9). We note that the 'extra' contact-metamorphic CO_2 would likely be liberated over longer time periods and not in a single pulse. However, the proportion of contact-metamorphic CO_2 outweighs the magmatic CO_2 in our calculations by ≥ factor 7, which is broadly consistent with the interpretation of present-day Vesuvius fumarole gas data that contain a high proportion of limestone derived-CO_2 (see above). Further uncertainties exist of course and relate to, e.g., the exact size of the aureole, different efficiencies of crustal carbonate conversion, the precise composition of the country rock, the temperature range of the magma involved, and the mechanisms and their respective time-scales to liberate the CO_2 (see e.g., Ganino et al., 2008; Ganino and Arndt, 2009; Svensen and Jamtveit, 2010; Jolis et al., 2013; Blythe et al., 2015). The amount of crustal CO_2 that directly contributed to the Pompeii and Pollena eruptions remains thus unknown, but the orders of magnitudes involved (see above) imply that crustal CO_2 was likely a key driver during the investigated eruptive events.

Given this realisation, we note that recent InSAR data allow for another possible effect of increased CO_2 fluxes in the Vesuvius volcanic system. Fluid-mechanical coupling of Campi Flegrei and Vesuvius during past eruptions, and especially during the last 16 years of satellite-monitored deformation episodes (Walter et al., 2014), now raises the possibility that syn-eruptive liberation of CO_2 at Vesuvius could translate into unrest at Campi Flegrei, or vice-versa. Because fluid travel-speeds of up to 300 m/d have been experimentally confirmed in crustal fractures (Zoback and Harjes, 1997; Shapiro et al., 2006) and because CO_2 is increasingly considered as a fault lubricant in active fracture systems (cf. Miller et al., 2004), such an interplay appears conceivable.

7. Conclusions

Petrological, mineralogical, major and trace elements, and especially stable isotope (C, O) data of igneous samples and contact-metamorphic xenoliths from Vesuvius volcanic system make a case for magma–carbonate interaction beneath the volcano before and during the Pompeii and Pollena eruptions. The high $\delta^{18}O$ values of the igneous samples, coupled with the large variability of O and C isotopes amongst the skarn sample suite (Fig. 5), record magma–crust interaction and explain associated conversion of original crustal carbonate to progressively more silica-rich skarn compositions (Fig. 8) (e.g., Fulignati et al., 2004; Gaeta et al., 2009; Mollo et al., 2010). Magma–crust interaction beneath Vesuvius likely occurs via a range of processes, including direct carbonate dissolution, calc-silicate formation and subsequent ingestion, and fluid metasomatism at wall-rock interfaces.

A contact aureole of originally pure limestone that forms a shell of for instance an extra 5% added to all three axes of an ellipsoidal magma reservoir, can liberate an amount of CO_2 seven times greater than that released by the magma in the contained reservoir (Fig. 9). Thus, a significant portion of the CO_2 involved in the explosive AD 79 and AD 472 eruptions might have been derived from contact metamorphic reactions.

Supplementary data to this article can be found online at http://dx.doi.org/10.1016/j.chemgeo.2015.09.003.

Acknowledgments

We like to thank to F. Rawoot for assistance during analysis at UCT and F.M. Deegan, A.K. Barker, S. Mollo, L. Dallai, L.S. Blythe and P. Younger for insightful discussions on earlier versions of the manuscript. We also thank C. Chauvel, N. Arndt, C.G. Barnes and an anonymous reviewer for their constructive comments that helped to greatly improve the manuscript. We are especially grateful to the Swedish Science Foundation (VR), the Royal Swedish Academy of Science (KVA), the Center for Natural Disaster Sciences (CNDS) at Uppsala University (UU), and the Istituto Nazionale di Geofisica e Vulcanologia (INGV) for generous financial or logistical support.

References

Aarnes, I., Svensen, H., Connolly, J.A.D., Podladchikov, Y.Y., 2010. How contact metamorphism can trigger global climate changes: Modeling gas generation around igneous sills in sedimentary basins. Geochim. Cosmochim. Acta 74 (24), 7179–7195. http://dx.doi.org/10.1016/j.gca.2010.09.011.

Aarnes, I., Fristad, K., Planke, S., Svensen, H., 2011a. The impact of host-rock composition on devolatilization of sedimentary rocks during contact metamorphism around mafic sheet intrusions. Geochem. Geophys. Geosyst. 12, 1–11. http://dx.doi.org/10.1029/2011GC003636 (Q10019).

Aarnes, I., Svensen, H., Polteau, S., Planke, S., 2011b. Contact metamorphic devolatilization of shales in the Karoo Basin South Africa, and the effects of multiple sill intrusions. Chem. Geol. 281, 181–194. http://dx.doi.org/10.1016/j.chemgeo.2010.12.007.

Abratis, J.C., Schmincke, H.-U., Hansteen, T.H., 2002. Composition and evolution of submarine volcanic rocks from the central and western Canary Islands. Int. J. Earth Sci. (Geol. Rundsch.) 91, 562–582.

Allard, P., Jean-Baptiste, P., D'Alessandro, W., Parello, F., Parisi, B., Flehoc, C., 1997. Mantle-derived helium and carbon in groundwaters and gases of Mount Etna, Italy. Earth Planet. Sci. Lett. 148, 501–516.

Arrighi, S., Principe, C., Rosi, M., 2001. Violent strombolian and subplinian eruptions at Vesuvius during post-1631 activity. Bull. Volcanol. 63, 126–150.

Auger, E., Gasparini, P., Virieux, J., Zollo, A., 2001. Seismic evidence of an extended magmatic sill under Mt. Vesuvius. Science 294, 1510–1512.

Auger, E., Virieux, J., Zollo, A., 2003. Locating and quantifying the seismic discontinuities in a complex medium through the migration and AVA analysis of reflected and converted waves: an application to the Mt Vesuvius volcano. Geophys. J. Int. 152, 486–496.

Aulinas, M., Civetta, L., Di Vito, M.A., Orsi, G., Gimeno, D., Férnandez Turiel, J.L., 2008. The "Pomici di Mercato" Plinian eruption of Somma-Vesuvius: magma chamber processes and eruption dynamics. Bull. Volcanol. 70 (7), 825–840. http://dx.doi.org/10.1007/s00445-007–0172-z.

Ayuso, R.A., De Vivo, B., Rolandi, G., Seal II, R.R., Paone, A., 1998. Geochemical and isotopic (Nd-Pb-Sr-O) variations bearing on the genesis of volcanic rocks from Vesuvius, Italy. J. Volcanol. Geotherm. Res. 82, 53–78.

Balcone-Boissard, H., Boudon, G., Ucciani, G., Villemant, B., Cioni, R., Civetta, L., Orsi, G., 2012. Magma degassing and eruption dynamics of the Avellino pumice Plinian eruption of Somma-Vesuvius (Italy). Comparison with the Pompeii eruption. Earth Planet. Sci. Lett. 331–332, 257–268.

Barberi, F., Leoni, L., 1980. Metamorphic carbonate ejecta from Vesuvius Plinian Eruptions: Evidence of the occurrence of shallow magma chambers. Bull. Volcanol. 43, 107–120.

Barberi, F., Bizouard, H., Clocchiatti, R., Metrich, N., Santacroce, R., Sbrana, A., 1981. The Somma-Vesuvius magma chamber: a petrological and volcanological approach. Bull. Volcanol. 44–3, 295–315.

Barnes, C.G., Prestvik, T., Sundvoll, B., Surratt, D., 2005. Pervasive assimilation of carbonate and silicate rocks in the Hortavær igneous complex, north-central Norway. Lithos 80, 179–199.

Barnes, C.G., Prestvik, T., Li, Y., McCulloch, L., Yoshinobu, A.S., Frost, C.D., 2009. Growth and zoning of the Hortavær intrusive complex, a layered alkaline pluton in the Norwegian Caledonides. Geosphere 5, 286–301. http://dx.doi.org/10.1130/GES00210.1.

Behrens, H., Misiti, V., Freda, C., Vetere, F., Botcharnikov, R.E., Scarlato, P., 2009. Solubility of H_2O and CO_2 in ultrapotassic melts at 1200 °C and 1250 °C and pressure from 50 to 500 MPa. Am. Mineral. 94, 105–120.

Belkin, H.E., De Vivo, B., Roedder, E., Cortini, M., 1985. Fluid inclusion geobarometry from ejected Mt. Somma-Vesuvius nodules. Am. Mineral. 70, 288–303.

Belkin, H.E., De Vivo, B., Török, K., Webster, J.D., 1998. Pre-eruptive volatile content, melt-inclusion chemistry, and microthermometry of interplinian Vesuvius lavas (pre-AD 1631). J. Volcanol. Geotherm. Res. 82, 79–95.

Bertagnini, A., Landi, P., Rosi, M., Vigliargio, A., 1998. The Pomici di Base plinian eruption of Somma-Vesuvius. J. Volcanol. Geotherm. Res. 83, 219–239 (PII S0377-0273(98)00025–0).

Bertagnini, A., Cioni, R., Guidoboni, E., Rosi, M., Neri, A., Boschi, E., 2006. Eruption early warning at Vesuvius: The A.D. 1631 lesson. Geophys. Res. Lett. 33, L18317. http://dx.doi.org/10.1029/2006GL027297.

Bindeman, I.N., 2008. Oxygen isotopes in mantle and crustal magmas as revealed by single crystal analysis. Rev. Mineral. Geochem. 69, 445–478.

Bindeman, I.N., Eiler, J.M., Yogodzinski, G.M., Tatsumi, Y., Stern, C.R., Grove, T.L., Portnyagin, M., Hoernle, K., Danyushevsky, L.V., 2005. Oxygen isotope evidence for slab melting in modern and ancient subduction zones. Earth Planet. Sci. Lett. 235, 480–496.

Bindeman, I.N., Schmitt, A.K., Valley, J.W., 2006. U-Pb zircon geochronology of silicic tuffs from the Timber Mountain/Oasis Valley caldera complex, Nevada: rapid generation of large volume magmas by shallow-level remelting. Contrib. Mineral. Petrol. 152, 649–665.

Blythe, L.S., Deegan, F.M., Freda, C., Jolis, E.M., Masotta, M., Misiti, V., Taddeucci, J., Troll, V.R., 2015. CO_2 bubble generation and migration during magma–carbonate interaction. Contrib. Mineral. Petrol. 169, 1–16.

Bohrson, W.A., Spera, F.J., 2001. Energy-constrained open-system magmatic processes II: Application of Energy-Constrained Assimilation-Fractional Crystallization (EC-AFC) model to magmatic systems. J. Petrol. 42, 1019–1041.

Borisova, A., Martel, C., Gouy, S., Pratomo, I., Sumarti, S., Toutain, J.-P., Bindeman, I.N., de Parseval, P., Metaxian, J.-P., Surono, 2013. Highly explosive 2010 Merapi eruption: Evidence for shallow-level crustal assimilation and hybrid fluid. J. Volcanol. Geotherm. Res. 261, 193–208.

Borthwick, J., Harmon, R.S., 1982. A note regarding ClF_3 as an alternative to BrF_5 for oxygen isotope analysis. Geochim. Cosmochim. Acta 46, 1665–1668.

Bowman, J.R., 1998. Stable-isotope systematics of skarns. Mineralogical Association of Canada Short Course 26, pp. 99–145.

Bowman, J.R., O'Neil, J.R., Essene, J.R., 1985. Contact skarn formation at Elkhorn, Montana, II: origin and evolution of C–O–H skarn fluids. Am. J. Sci. 285, 621–660.

Brocchini, D., Principe, C., Castradori, D., Laurenzi, M.A., Gorla, L., 2001. Quaternary evolution of the southern sector of the Campanian Plain and early Somma-Vesuvius activity: insights from Trecase 1 well. Mineral. Petrol. 73, 67–91.

Bruno, P.P., Cippitelli, G., Rapolla, A., 1998. Seismic study of the Mesozoic carbonate basement around Mt. Somma-Vesuvius, Italy. J. Volcanol. Geotherm. Res. 84, 311–322.

Chadwick, J.P., Troll, V.R., Ginibre, C., Morgan, D., Gertisser, R., Waight, T.E., Davidson, J.P., 2007. Carbonate assimilation at Merapi volcano, Java, Indonesia: Insights from crystal isotope stratigraphy. J. Petrol. 48, 1793–1812.

Chiodini, G., Marini, L., Russo, M., 2001. Geochemical evidence for the existence of high-temperature hydrothermal brines at Vesuvio volcano, Italy. Geochim. Cosmochim. Acta 65, 2129–2147.

Cioni, R., Civetta, L., Marianelli, P., Metrich, N., Santacroce, R., Sbrana, A., 1995. Compositional layering and syn-eruptive mixing of a periodically refilled shallow magma chamber: the AD 79 Plinian eruption of Vesuvius. J. Petrol. 36, 739–776.

Cioni, R., 2000. Volatile content and degassing processes in the AD 79 magma chamber at Vesuvius (Italy). Contrib. Mineral. Petrol. 140, 40–54.

Cioni, R., Bertagnini, A., Santacroce, R., Andronico, D., 2008. Explosive activity and eruption scenarios at Somma-Vesuvius (Italy): Towards a new classification scheme. J. Volcanol. Geotherm. Res. 178, 331–346.

Cioni, R., Marianelli, P., Santacroce, R., 1998. Thermal and compositional evolution of the shallow magma chambers of Vesuvius: Evidence from pyroxene phenocrysts and melt inclusions. J. Geophys. Res. 103, 18277–18294.

Cioni, R., Santacroce, R., Sbrana, A., 1999. Pyroclastic deposits as a guide for reconstructing the multi-stage evolution of the Somma-Sesuvius caldera. Bull. Volcanol. 60, 207–222.

Cioni, R., Sulpizio, R., Garruccio, N., 2003. Variability of the eruption dynamics during a Subplinian event: the Greenish Pumice eruption of Somma-Vesuvius (Italy). J. Volcanol. Geotherm. Res. 124 (1–2), 89–114.

Civetta, L., Galati, R., Santacroce, R., 1991. Magma mixing and convective compositional layering within the Vesuvius magma chamber. Bull. Volcanol. 53, 287–300.

Civetta, L., D'Antonio, M., de Lorenzo, S., Di Renzo, V., Gasparini, P., 2004. Thermal and gochemical constraints on the 'deep' magmatic structure of Mt. Vesuvius. J. Volcanol. Geotherm. Res. 133, 1–12.

Coplen, T.B., Kendall, C., Hopple, J., 1983. Intercomparison of stable isotope reference samples. Nature 302, 236–238.

Cortini, M., Hermes, O.D., 1981. Sr isotopic evidence for a multi-source origin of the potassic magmas in the Neapolitan area (S. Italy). Contrib. Mineral. Petrol. 77, 47–55.

Coulson, I.M., Westphal, M., Anderson, R.G., Kyser, T.K., 2007. Concomitant skarn and syenitic magma evolution at the margins of the Zippa Mountain pluton. Mineral. Petrol. 90, 199–221.

D'Antonio, M., Civetta, L., Orsi, G., Pappalardo, L., Piochi, M., Carandente, A., De Vita, S., Di Vito, M.A., Isaia, R., Southon, J., 1999. The present state of the magmatic system of the Campi Flegrei caldera based on the reconstruction of its behaviour in the past 12 ka. J. Volcanol. Geotherm. Res. 91, 247–268.

D'Argenio, B., Pescatore, T., Scandone, P., 1973. Schema Geologico dell'Appennino Meridionale (Campania e Lucania). Paper presented at Moderne vedute della geologia dell'Appennino. Accad. Naz. dei Lincei, Rome.

Dallai, L., Cioni, R., Boschi, C., D'Oriano, C., 2011. Carbonate-derived CO_2 purging magma at depth: Influence on the eruptive activity of Somma-Vesuvius, Italy. Earth Planet. Sci. Lett. 310, 84–95.

Dallai, L., Freda, C., Gaeta, C., 2004. Oxygen isotope geochemistry of pyroclastic clinopyroxene monitors carbonate contributions to Roman-type ultrapotassic magmas. Contrib. Mineral. Petrol. 148, 247–263.

Davidson, J.P., Hora, J.M., Garrison, J.M., Dungan, M.A., 2005. Crustal forensic in arc magmas. J. Volcanol. Geotherm. Res. 140, 157–170.

Davidson, J.P., McMillan, N.J., Moorbath, S., Wörner, G., Russell, S.H., Lopez-Escobar, L., 1990. The Nevados de Payachata volcanic region (18° S/69° W, N. Chile) II. Evidence for widespread crustal involvement in Andean magmatism. Contrib. Mineral. Petrol. 105, 412–432.

Deer, W.A., Howie, R.A., Zussman, J., 1992. An introduction to the rock-forming minerals. Longman Scientific and Technical, 2nd ed. Wiley, New York, NY.

De Lorenzo, S., Di Renzo, V., Civetta, L., D'Antonio, M., Gasparini, P., 2006. Thermal model of the Vesuvius magma chamber. Geophys. Res. Lett. 33, L17302.

De Paolo, D.J., 1981. Trace element and isotopic effects of combined wallrock assimilation and fractional crystallization. Earth Planet. Sci. Lett. 53, 189–202.

Deegan, F.M., Troll, V.R., Freda, C., Misiti, V., Chadwick, J.P., 2011. Fast and furious: crustal CO_2 release at Merapi volcano, Indonesia. Geol. Today 27, 63–64.
Deegan, F.M., Troll, V.R., Freda, C., Misiti, V., Chadwick, J.P., McLeod, C.L., Davidson, J.P., 2010. Magma–carbonate interaction processes and associated CO_2 release at Merapi volcano, Indonesia: insights from experimental petrology. J. Petrol. 51, 1027–1051.
De Matteis, R., Latorre, D., Zollo, A., Virieux, J., 2000. 1D P-velocity models of Mt. Vesuvius volcano from the inversion of TomoVes96 first arrival time data, Pure Appl. Geophys. 157, 1643–1661.
De Vivo, B., Torok, K., Ayuso, R.A., Lima, A., Lirer, L., 1995. Fluid inclusion evidence for magmatic/saline/CO_2 immiscibility and geochemistry of alkaline xenoliths from Ventotene Island, Italy. Geochim. Cosmochim. Acta 59, 2941–2953.
Del Moro, A., Fulignati, P., Marianelli, P., Sbrana, A., 2001. Magma contamination by direct wall rock interaction: constraints from xenoliths from the wall of carbonate-hosted magma chamber (Vesuvius 1944 eruption). J. Volcanol. Geotherm. Res. 112, 15–24.
Del Pezzo, E., Bianco, F., De Siena, L., Zollo, A., 2006. Small scale shallow attenuation structure at Mt. Vesuvius, Italy. Phys. Earth Planet. Inter. 157, 257–268.
Di Renzo, V., Di Vito, M.A., Arienzo, I., Carandente, A., Civetta, L., D'Antonio, M., Giordano, F., Orsi, G., Tonarini, S., 2007. Magmatic history of Somma-Vesuvius on the basis of new geochemical and isotopic data from a deep borehole (Camaldoli della Torre). J. Petrol. 48, 753–784.
Di Rocco, T., Freda, C., Gaeta, M., Mollo, S., Dallai, L., 2012. Magma chambers emplaced in carbonate substrate: petrogenesis of skarn and cumulate rocks and implications for CO_2 degassing in volcanic areas. J. Petrol. 53, 2307–2332.
Donoghue, E., Troll, V.R., Harris, C., O'Halloran, A., Walter, T.R., Pérez Torrado, F.J., 2008. Low-temperature hydrothermal alteration of intra-caldera tuffs, Miocene Tejeda caldera, Gran Canaria, Canary Islands. J. Volcanol. Geotherm. Res. 176, 551–564.
Dyer, B., Lee, C.A., Leeman, W.P., Tice, M., 2011. Open-system behavior during pluton-wall-rock interaction as constrained from a study of endoskarns in the Sierra Nevada batholith, California. J. Petrol. 52, 1987–2008.
Eiler, J.M., Farley, K.A., Valley, J.W., Hofmann, A.W., Stolper, E.M., 1996. Oxygen isotope constraints on the sources of Hawaiian volcanism. Earth Planet. Sci. Lett. 144, 453–467.
Fagereng, Å., Harris, C., La Grange, M., Stevens, G., 2008. Stable isotope study of the Archean rocks of the Vredefort impact structure, central Kaapvaal Craton, South Africa. Contrib. Mineral. Petrol. 155, 63–78.
Freda, C., Gaeta, M., Giaccio, B., Marra, F., Palladino, D.M., Scarlato, P., Sottili, G., 2011. CO_2-driven large mafic explosive eruptions: The Pozzolane Rosse case study from the Colli Albani Volcanic District (Italy). Bull. Volcanol. 73, 241–256.
Freda, C., Gaeta, M., Misiti, V., Mollo, S., Dolfi, D., Scarlato, P., 2008. Magma–carbonate interaction: an experimental study on ultrapotassic rocks from Alban Hills (Central Italy). Lithos 101, 397–415.
Freda, C., Gaeta, M., Palladino, D.M., Trigila, R., 1997. The Villa Senni Eruption (Alban Hills, central Italy): the role of H_2O and CO_2 on the magma chamber evolution and on the eruptive scenario. J. Volcanol. Geotherm. Res. 78, 103–120.
Fulignati, P., Marianelli, P., Sbrana, A., 1998. New insights on the thermometamorphic-metasomatic magma chamber shell of the 1944 eruption of Vesuvius. Acta Vulcanol. 10 (1), 47–54.
Fulignati, P., Marianelli, P., Sbrana, A., 2000. Glass-bearing felsic nodules from the crystallisation sidewalls of the 1944 Vesuvius magma chamber. Mineral. Mag. 64, 481–496.
Fulignati, P., Kamenetsky, V.S., Marianelli, P., Sbrana, A., Mernagh, T.P., 2001. Melt inclusion record of immiscibility between silicate, hydrosaline, and carbonate melts: Application to skarn genesis at Mount Vesuvius. Geology 29, 1043–1046.
Fulignati, P., Marianelli, P., Santacroce, R., Sbrana, A., 2004. Probing the Vesuvius magma chamber-host rock interface through xenoliths. Geol. Mag. 141, 417–428.
Fulignati, P., Panichi, C., Sbrana, A., Caliro, S., Gioncada, A., Del Moro, A., 2005a. Skarn formation at the walls of the 79 AD magma chamber of Vesuvius (Italy): Mineralogical and isotopic constraints. N. Jb. Mineral. (Abh.) 181, 53–66.
Fulignati, P., Kamenetsky, V., Marianelli, P., Sbrana, A., 2005b. Fluid inclusions evidence of second immiscibility within magmatic fluids (79 AD eruption of Mt. Vesuvius). Period. Miner. 74, 43–54.
Fulignati, P., Marianelli, P., 2007. Tracing volatile exsolution within the 472 AD "Pollena" magma chamber of Vesuvius (Italy) from melt inclusion investigation. J. Volcanol. Goetherm. Res. 161, 289–302.
Fulignati, P., Kamenetsky, V., Marianelli, P., Sbrana, A., Meffre, S., 2011. First insights on the metallogenic signature of magmatic fluids exsolved from the active magma chamber of Vesuvius (AD 79 "Pompei" eruption). J. Volcanol. Geotherm. Res. 200, 223–233.
Fulignati, P., Kamenetsky, V., Marianelli, P., Sbrana, A., 2013. PIXE mapping on multiphase fluid inclusions in endoskarns xenoliths of AD 472 eruption of Vesuvius (Italy). Period. Miner. 82, 291–297.
Gaeta, M., Di Rocco, T., Freda, C., 2009. Carbonate assimilation in open magmatic systems: the role of melt-bearing skarns and cumulate forming processes. J. Petrol. 50, 361–385.
Ganino, C., Arndt, N.T., 2009. Climate changes caused by degassing of sediments during the emplacement of large igneous provinces. Geology 37, 323–326.
Ganino, C., Arndt, N., Zhou, N.T., Gaillard, F., Chauvel, C., 2008. Interaction of magma with sedimentary wall rock and magmatic ore genesis in the Panzhihua mafic intrusion, SW China. Mineral. Deposita 43, 677–694.
Gilg, H.A., Lima, A., Somma, R., Belkin, H.E., De Vivo, B., Ayuso, R.A., 2001. Isotope geochemistry and fluid inclusions study of skarns from Vesuvius. Mineral. Petrol. 73, 145–176.
Goff, F., Love, S.P., Warren, R.G., Counce, D., Obenholzner, J., Siebe, C., Schmidt, S.C., 2001. Passive infrared remote sensing evidence for large, intermittent CO_2 emissions at Popcatépetl volcano, Mexico. Chem. Geol. 177, 133–156.
Harmon, R.S., Hoefs, J., 1995. Oxygen isotope heterogeneity of the mantle deduced from global ^{18}O systematics of basalt from different geotectonic settings. Contrib. Mineral. Petrol. 120, 95–114.
Harris, C., Ashwal, L.D., 2002. The origin of low $\delta^{18}O$ granites and related rocks from the Seychelles. Contrib. Mineral. Petrol. 143, 366–376.
Heap, M.J., Mollo, S., Vinciguerra, S., Lavallée, Y., Hess, K.-U., Dingwell, D.B., Baud, P., Iezzi, G., 2013. Thermal weakening of the carbonate basement under Mt. Etna volcano (Italy): Implications for volcano instability. J. Volcanol. Geotherm. Res. 250, 42–60.
Hermes, O.D., Cornell, W.C., 1981. Quenched crystal mush and associated magma compositions as indicated by intercumulus glasses from Mt Vesuvius, Italy. J. Volcanol. Geotherm. Res. 9, 133–149.
Hildreth, W., Moorbath, S., 1988. Crustal contributions to arc magmatism in the Andes of Central Chile. Contrib. Mineral. Petrol. 98, 455–489.
Hilton, D.R., Fischer, T.P., Marty, B., 2002. Noble gases and volatile recycling at subduction zones. In: Porcelli, D., Ballentine, C.J., Wieler, R. (Eds.), Noble Gases in Geochemistry and Cosmochemistry. Mineralogical Society of America. Rev. Mineral. Geochem. 47, pp. 319–370.
Hoefs, J., 1996. Stable Isotopes. Springer Verlag, Berlin, p. 201.
Iacono-Marziano, G., Gaillard, F., Pichavant, M., 2007. Limestone assimilation and the origin of CO_2 emissions at the Alban Hills (Central Italy): Constraints from experimental petrology. J. Volcanol. Geotherm. Res. 166, 91–105.
Iacono-Marziano, G., Gaillard, F., Pichavant, M., 2008. Limestones assimilation by basaltic magmas: an experimental re-assessment and application to Italian volcanoes. Contrib. Mineral. Petrol. 155, 719–738.
Iacono-Marziano, G., Gaillard, F., Scaillet, B., Pichavant, M., Chiodini, G., 2009. Role of non-mantle CO_2 in the dynamics of volcano degassing: the Mount Vesuvius example. Geology 37, 319–322.
Iannace, A., Capuano, M., Galluccio, L., 2011. Dolomites and dolomites" in Mesozoic platform carbonates of the Southern Apennines: Geometric distribution, petrography and geochemistry. Palaeogeogr. Palaeoclimatol. Palaeoecol. 310, 324–339.
Ippolito, F., D'Argenio, B., Pescatore, T., Scandone, P., 1975. Structural-stratigraphic units and tectonic framework of southern Apennines, Geology of Italy, edited by C. Squyres, pp. 11, Lybian Soc. of Earth Sci., Tripoli, Libya Arab Republic.
Ito, E., White, W.M., Göpel, C., 1987. The O, Sr, Nd and Pb isotope geochemistry of MORB. Chem. Geol. 62, 157–176.
Javoy, M., Pineau, F., Delorme, H., 1986. Carbon and nitrogen isotopes in the mantle. Chem. Geol. 57, 41–62.
Jeffery, A., Gertisser, R., Troll, V.R., Jolis, E.M., Dahren, B., Harris, C., Tindle, A.G., Preece, K., O'Driscoll, B., Humaida, H., Chadwick, J.P., 2013. The pre-eruptive magma plumbing system of the 2007–2008 dome-forming eruption of Kelut volcano, Indonesia. Contrib. Mineral. Petrol. 166, 275–305.
Jolis, E.M., Freda, C., Troll, V.R., Deegan, F.M., Blythe, L.S., McLeod, C.L., Davidson, J.P., 2013. Experimental simulation of magma–carbonate interaction beneath Mt. Vesuvius, Italy. Contrib. Mineral. Petrol. 166, 1335–1353. http://dx.doi.org/10.1007/s00410-013-0931-0.
Lackey, J.S., Valley, J.W., Hinke, H.J., 2006. Deciphering the source and contamination history of peraluminous magmas using $\delta^{18}O$ of accessory minerals: Examples from garnet-bearing plutons of the Sierra Nevada batholith. Contrib. Mineral. Petrol. 151, 20–44.
Landi, P., Bertagnini, A., Rosi, M., 1999. Chemical zoning and crystallization mechanisms in the magma chamber of the Pomici di Base plinian eruption of Somma-Vesuvius (Italy). Contrib. Mineral. Petrol. 135, 179–197.
Lentz, D.R., 1999. Carbonatite genesis: A re-examination of the role of intrusion-related pneumatolytic skarn processes in limestone melting. Geology 27, 335–338.
Lima, A., De Vivo, B., Fedele, L., Sintoni, F., Milia, A., 2007. Geochemical variations between the 79 AD and 1944 AD Somma-Sesuvius volcanic products: Constraints on the evolution of the hydrothermal system based on fluids and melt inclusions. Chem. Geol. 237, 401–417.
McCrea, J.M., 1950. On the isotopic chemistry of carbonates and a paleotemperature scale. J. Chem. Phys. 18, 849–857.
Marianelli, P., Métrich, N., Sbrana, A., 1999. Shallow and deep reservoirs involved in magma supply of the 1944 eruption of Vesuvius. Bull. Volcanol. 61, 48–63.
Marianelli, P., Métrich, N., Santacroce, R., Sbrana, A., 1995. Mafic magma batches at Vesuvius: a glass inclusion approach to the modalities of feeding stratovolcanoes. Contrib. Mineral. Petrol. 120, 159–169.
Martin, L.H.J., Schmidt, M.W., Mattsson, H.B., Ulmer, P., 2012. Element partitioning between immiscible carbonatite-kamafugite melts with application to the Italian ultrapotassic suite. Chem. Geol. 320-321, 96–112.
Mattey, D., Lowry, D., Macpherson, C., 1994. Oxygen isotope composition of mantle peridotite. Earth Planet. Sci. Lett. 128, 231–241.
Meinert, L.D., 1992. Skarns and skarn deposits. Geosci. Can. 19, 145–162.
Mele, D., Sulpizio, R., Dellino, P., La Volpe, L., 2011. Stratigraphy and eruptive dynamics of a pulsating Plinian eruption of Somma-Vesuvius: the Pomici di Mercato (8900 years B.P.). Bull. Volcanol. 73, 257–278.
Melezhik, V.A., Fallick, A.E., Smirnov, Y.P., Yakovlev, Y.N., 2003. Fractionation of carbon and oxygen isotopes in ^{13}C-rich Palaeoproterozoic dolostones in the transition from medium-grade to high-grade greenschist facies: a case study from the Kola Superdeep Drillhole. J. Geol. Soc. (London, U.K.) 160, 71–82.
Miller, S.A., Collettini, C., Chiaraluce, L., Cocco, M., Barchi, M., Kaus, B.J.P., 2004. Aftershocks driven by a high-pressure CO_2 source at depth. Nature 427, 724–727.
Mollo, S., Gaeta, M., Freda, C., Di Rocco, T., Misiti, V., Scarlato, V., 2010. Carbonate assimilation in magmas: A reappraisal based on experimental petrology. Lithos 114, 503–514.
Mollo, S., Heap, M.J., Iezzi, G., Hess, K.-U., Scarlato, P., Dingwell, D.B., 2012. Volcanic edifice weakening via decarbonation: A self-limiting process? Geophys. Res. Lett. 39, L15307. http://dx.doi.org/10.1029/2012GL052613.

Mantovani, M.S.M., Hawkesworth, C.J., 1990. An inversion approach to assimilation and fractional crystallization processes. Contrib. Mineral. Petrol. 105, 289–302.

Moretti, R., Arienzo, I., Orsi, G., Civetta, L., D'Antonio, M., 2013. The Deep Plumbing System of Ischia: a Physico-chemical Window on the Fluid-saturated and CO_2-sustained Neapolitan Volcanism (Southern Italy). J. Petrol. 54 (5), 951–984. http://dx.doi.org/10.1093/petrology/egt002.

Morgan, D.J., Blake, S., Rogers, N.W., De Vivo, B., Rolandi, G., Davidson, J.P., 2006. Magma chamber recharge at Vesuvius in the century prior to the eruption of A.D. 79. Geology 34, 845–848.

Nabelek, P.I., Labotka, T.C., O'Neil, J.R., Papike, J.J., 1984. Contrasting fluid/rock interaction between the Notch Peak granitic intrusion and argillites and limestones in western Utah: evidence from stable isotopes and phase assemblages. Contrib. Mineral. Petrol. 86, 25–34.

Orhan, A., Mutlu, H., Fallick, A.E., 2011. Fluid infiltration effects on stable isotope systematics of the Susurluk skarn deposit, NW Turkey. J. Asian Earth Sci. 40, 550–568.

Orsi, G., De Vita, S., Di Vito, M., Isaia, R., Nave, R., Heiken, G., 2003. Facing volcanic and related hazards in the Neapolitan area. In: Heiken, G., Fakundiny, R., Sutter, J. (Eds.), Earth Sciences in the Cities: A Reader. Am Geophys Un, Sp Publ Series 56, pp. 121–170.

Paone, A., 2006. The geochemical evolution of the Mt. Somma-Vesuvius volcano. Mineral. Petrol. 87, 53–80.

Pappalardo, L., Civetta, L., D'Antonio, M., Deino, A., Di Vito, M., Orsi, G., Carandente, A., de Vita, S., Isaia, R., Piochi, M., 1999. Chemical and Sr-isotopical evolution of the Phlegraean magmatic system before the Campanian Ignimbrite and the Neapolitan Yellow Tuff eruptions. J. Volcanol. Geotherm. Res. 91, 141–166.

Pappalardo, L., Piochi, M., D'Antonio, M., Civetta, L., Petrini, R., 2002. Evidence for multistage magmatic evolution during the past 60 kyr at Campi Flegrei (Italy) deduced from Sr, Nd and Pb isotope data. J. Petrol. 43, 1415–1434.

Pappalardo, L., Piochi, M., Mastrolorenzo, G., 2004. The 3550 year BP-1944 A.D. magma-plumbing system of Somma-Vesuvius: constraints on its behaviour and present state through a review of Sr-Nd isotope data. Ann. Geophys. 47, 1471–1483.

Pappalardo, L., Mastrolorenzo, G., 2010. Short residence times for alkaline Vesuvius magmas in a multi-depth supply system: Evidence from geochemical and textural studies. Earth Planet. Sci. Lett. 296, 133–143.

Parente, M., Frijia, G., Di Lucia, M., 2007. Carbon-isotope stratigraphy of Cenomanian-Turonian platform carbonates from the southern Apennines (Italy): a chemo-stratigraphic approach to the problem of correlation between shallow-water and deep-water successions. Geol. Soc. Lond. J 164, 609–620.

Peccerillo, A., 1999. Multiple mantle metasomatism in central-southern Italy: Geochemical effects, timing and geodynamic implications. Geology 27, 315–318.

Peccerillo, A., 2001. Geochemical similarities between the Vesuvius, Phlegraean Fields and Stromboli volcanoes: petrogenetic, geodynamic and volcanological implications. Mineral. Petrol. 73, 93–105.

Peccerillo, A., 2005. Plio-Quaternary Volcanism in Italy. Petrology, Geochemistry, Geodynamics. Springer Berlin Heidelberg, New York, p. 365.

Pichavant, M., Scaillet, B., Pommier, A., Iacono-Marziano, G., Cioni, R., 2014. Nature and evolution of primitive Vesuvius magmas: an experimental study. J. Petrol. 55, 2281–2310.

Piochi, M., Ayuso, R.A., De Vivo, B., Somma, R., 2006. Crustal contamination and crystal entrapment during polybaric magma evolution at Mt. Somma-Vesuvius volcano, Italy: Geochemical and Sr isotope evidence. Lithos 86, 303–329.

Rittmann, A., 1962. Volcanoes and Their Activity. John Wiley and Sons, New York, p. 305.

Sano, Y., Marty, B., 1995. Origin of carbon in fumarolic gas from island arcs. Chem. Geol. 119, 265–274. http://dx.doi.org/10.1016/0009-2541(94)00097-R.

Santacroce, R. (Ed.), 1987. Somma-VesuviusQuaderni della Ricerca Scientifica 114, 8. CNR, pp. 1–251.

Santacroce, R., Cioni, R., Marianelli, P., Sbrana, A., Sulpizio, R., Zanchetta, G., Donahue, D.J., Joron, J.L., 2008. Age and whole rock-glass compositions of proximal pyroclastics from the major explosive eruptions of Somma-Vesuvius: A review as a tool for distal tephrostratigraphy. J. Volcanol. Geotherm. Res. 177, 1–18.

Scaillet, B., Pichavant, M., Cioni, R., 2008. Upward migration of Vesuvius magma chamber over the past 20.000 years. Nature 455, 216–219.

Scandone, P., 1982. Structure and evolution of the Calabrian arc. Earth Evol. Sci. 2 (3), 172–180.

Schaaf, P., Stimac, J., Siebe, C., Macias, J.L., 2005. Geochemical evidence for mantle origin and crustal processes in volcanic rocks from Popocatépelt and surrounding monogenetic volcanoes, central Mexico. J. Petrol. 46, 1243–1282.

Scheibner, B., Wörner, G., Civetta, L., Stosch, H.-G., Simon, K., Kronz, A., 2007. Rare earth element fractionation in magmatic Ca-rich garnets. Contrib. Mineral. Petrol. 154, 55–74. http://dx.doi.org/10.1007/s00410-006-0179-z.

Schutte, K.G., 1978. Crustal structure of southern Italy. In: Closs, H., Roeder, D.R., Schmidt, K. (Eds.), Alps, Apennines and Hellenides. Scweizerbart, Stuttgart, Germany, pp. 315–327.

Self, S., Widdowson, M., Thordarsson, T., Jay, A.E., 2006. Volatile fluxes during flood basalt eruptions and potential effects on the global environment: a Deccan perspective. Earth Planet. Sci. Lett. 248, 518–532.

Sevink, J., van Bergen, M.J., van der Plicht, J., Feiken, H., Anastasia, C., Huizinga, A., 2011. Robust date for the Bronze Age Avellino eruption (Somma-Vesuvius): 3945 ± 10 calBP (1995 ± 10 calBP). Quat. Sci. Rev. 30, 1035–1046.

Shapiro, S.A., Kummerow, J., Dinske, C., Asch, G., Rother, E., Erzinger, J., Kümpel, H.-J., Kind, R., 2006. Fluid induced seismicity guided by a continental fault: Injection experiment of 2004/2005 at the German Deep Drilling Site (KTB). Geophys. Res. Lett. 33, L01309. http://dx.doi.org/10.1029/1005GL024659.

Sharp, Z., 2007. Principles of stable isotope geochemistry 2007. Prentice Hall, New York, p. 360.

Sigurdsson, H., Carey, S., Cornell, W., Pescatore, T., 1985. The eruption of Vesuvius in 79 AD. Natl. Geogr. Res. 1, 332–387.

Somma, R., Ayuso, R.A., De Vivo, B., Rolandi, G., 2001. Major, trace element and isotope geochemistry (Sr-Nd-Pb) of interplinian magmas from Mt. Somma-Vesuvius (Southern Italy). Mineral. Petrol. 73, 121–143.

Spera, F.J., Bohrson, W.A., 2001. Energy-constrained open-system magmatic processes I: general model and energy-constrained assimilation and fractional crystallization (EC-AFC) formulation. J. Petrol. 42, 999–1018.

Sulpizio, R., Bonasia, R., Dellino, P., Mele, D., Di Vito, M.A., La Volpe, L., 2010a. The Pomici di Avellino eruption of Somma–Vesuvius (3.9 ka BP). Part II: sedimentology and physical volcanology of pyroclastic density current deposits. Bull. Volcanol. 72, 559–577. http://dx.doi.org/10.1007/s00445-009-0340-4.

Sulpizio, R., Cioni, R., Di Vito, M.A., Mele, D., Bonasia, R., Dellino, P., 2010b. The Pomici di Avellino eruption of Somma-Vesuvius (3.9 ka BP). Part I: stratigraphy, compositional variability and eruptive dynamics. Bull. Volcanol. 72, 539–558. http://dx.doi.org/10.1007/s00445-009-0339-x.

Sulpizio, R., Mele, D., Dellino, P., La Volpe, L., 2005. A complex, Subplinian-type eruption from low-viscosity, phonolitic to tephri-phonolitic magma: the AD 472 (Pollena) eruption of Somma-Vesuvius, Italy. Bull. Volcanol. 67, 743–767.

Svensen, H., Jamtveit, B., 2010. Metamorphic fluids and global environmental changes. Elements 6, 179–182. http://dx.doi.org/10.2113/gselements.6.3.179.

Taylor, B.E., 1986. Magmatic volatiles: isotopic variation of C, H, and S. In: Valley, J.W., Taylor, H.P., O'Neil, J.R. (Eds.), Stable isotopes in high temperature geological processes. Rev. Mineral. 16, 185–225.

Taylor, B.E., Bucher-Nurminen, K., 1986. Oxygen and carbon isotope and cation geochemistry of metasomatic carbonates and fluids – Bergell aureole, Northern Italy. Geochim. Cosmochim. Acta 50, 1267–1279.

Taylor, B.E., O'Neil, J.R., 1977. Stable isotope studies of metasomatic Ca-Fe-Al-Si skarns and associated metamorphic and igneous rocks, Osgood Mountains, Nevada. Contrib. Mineral. Petrol. 63, 1–49.

Taylor, H.P., Sheppard, S.M.F., 1986. Igneous rocks I, Processes of isotopic fractionation and isotope systematics. In: Valley, J.W., Taylor, H.P., O'Neil, J.R. (Eds.), Stable isotopes in high temperature geological processes. Min Soc Am Rev in Min 16, pp. 227–271.

Tedesco, D., 1997. Systematic variations in the $^3He/^4He$ ratio and carbon of fumarolic fluids from active volcanic areas in Italy: evidence for radiogenic ^4He and crustal carbon additions by the subducting African plate? Earth Planet. Sci. Lett. 151, 255–269.

Troll, V.R., Chadwick, J.P., Ellam, R., McDonnell, S., Emeleus, C.H., Meighan, I., 2005. Sr and Nd isotope evidence for successive crustal contamination of ring-dyke magmas in the Slieve Gullion Igneous Centre, Ireland. Special issue invited 'Magma chamber dynamics'. Geol. Mag. 142, 659–668.

Troll, V.R., Deegan, F.M., Jolis, E.M., Harris, C., Chadwick, J.P., Gertisser, R., Schwarzkopf, L.M., Borisova, A.Y., Bindeman, I.N., Sumarti, S., Preece, K., 2013. Magmatic differentiation processes at Merapi Volcano: inclusions petrology and oxygen isotopes. J. Volcanol. Res. 261, 38–49. http://dx.doi.org/10.1016/j.jvolgeores.2012.11.001.

Troll, V.R., Hilton, D.R., Jolis, E.M., Chadwick, J.P., Blythe, L.S., Deegan, F.M., Schwarzkopf, L.M., Zimmer, M., 2012. Crustal CO_2 liberation during the 2006 eruption and earthquake events at Merapi volcano, Indonesia. Geophys. Res. Lett. 39, L11302. http://dx.doi.org/10.1029/2012GL051307.

Troll, V.R., Schmincke, H.-U., 2002. Magma Mixing and Crustal Recycling Recorded in Ternary Feldspar from Compositionally Zoned Peralkaline Ignimbrite 'A', Gran Canaria, Canary Islands. J. Petrol. 43, 243–270.

Turi, B., Taylor, H.P., 1976. Oxygen isotopes studies of potassic volcanic rocks of the Roman Provenance, Central Italy. Contrib. Mineral. Petrol. 55, 1–31.

Valley, J.W., 1986. Stable isotope geochemistry of metamorphic rocks. In: Valley, J.W., Taylor, H.P., O'Neil, J.R. (Eds.), Stable isotopes in high temperature geological processes. Min Soc Am Rev in Min 16, pp. 445–490.

Valley, J.W., Bindeman, I.N., Peck, W.H., 2003. Empirical calibration of oxygen isotope fractionation in zircon. Geochim. Cosmochim. Acta 67, 3257–3266.

Vennemann, T.W., Smith, H.S., 1990. The rate and temperature of reaction of CLF_3 with silicate minerals, and their relevance to oxygen isotope analysis. Chem. Geol. 86, 83–88.

Walker, J.A., Mickelson, J.E., Thomas, R.B., Patino, L.C., Cameron, B., Carr, M.J., Feigenson, M.D., Edwards, R.L., 2007. U-series disequilibria in Guatemalan lavas, crustal contamination, and implications for magma genesis along the Central American subduction zone. J. Geophys. Res. 112, B06205. http://dx.doi.org/10.1029/2006JB004589.

Walter, T.A., Shirzaei, M., Manconi, A., Solaro, G., Pepe, A., Manzo, M., Sansosti, E., 2014. Possible coupling of Campi Flegrei and Vesuvius as revealed by InSAR time series, correlation analysis and time dependent modeling. J. Volcanol. Geotherm. Res. 280, 104–110.

Wallace, P.J., 2005. Volatiles in subduction zone magmas; concentrations and fluxes based on melt inclusion and volcanic gas data. J. Volcanol. Geotherm. Res. 140, 217–240.

Watson, B.E., Sneeringer, M.A., Ross, A., 1982. Diffusion of dissolved carbonate in magmas: experimental results and applications. Earth Planet. Sci. Lett. 61, 346–358.

Webster, J.D., De Vivo, B., Tappen, C., 2003. Volatiles, magmatic degassing and eruptions of Mt. Somma–Vesuvius: Constraints from silicate melt inclusions, Cl and H_2O solubility experiments and modeling. Dev. Volcanol. 5, 207–226.

Weber, J.N., Woodhead, P.M.J., 1969. Factors affecting the carbon and oxygen isotopic composition of marine carbonate sediments-II. Heron Island, Great Barrier Reef, Australia. Geochim. Cosmochim. Acta 33, 19–38.

Wenzel, T., Baumgartner, L.P., Brügmann, G.E., Konnikov, E.G., Kislov, E.V., Orsoev, D.A., 2001. Contamination of mafic magma by partial melting of dolomitic xenoliths. Terra Nova 13, 197–202.

Wenzel, T., Baumgartner, L., Brügmann, G., Konnikov, E.G., Kislov, E.V., 2002. Partial melting and assimilation of dolomitic xenoliths by mafic magma: the Ioko-Dovyren Intrusion (North Baikal Region, Russia). J. Petrol. 43, 2049–2074.

Wilson, M., 1997. Igneous petrogenesis. Chapman and Hall, London, pp. 1–456.

Zheng, Y.F., 1993. Calculation of oxygen isotope fractionation in anhydrous silicate minerals. Geochim. Cosmochim. Acta 57, 1079–1091.

Zoback, M.D., Harjes, H.-P., 1997. Injection-induced earthquakes and crustal stress at 9 km depth at the KTB deep drilling site, Germany. J. Geophys. Res. 102 (B8), 18477–18491.

Zollo, A., Gasparini, P., Virieux, J., Biella, G., Boschi, E., Capuano, P., De Franco, R., Dell'Aversana, P., De Matteis, R., De Natale, G., Iannaccone, G., Guerra, I., Le Meur, H., Mirabile, L., 1998. An image of Mt. Vesuvius obtained by 2D seismic tomography. J. Volcanol. Geotherm. Res. 82, 161–173.

Zollo, A., Gasparini, P., Virieux, J., Le Meur, H., De Natale, G., Biella, G., Boschi, E., Capuano, P., De Franco, R., Dell'Aversana, P., De Matteis, R., Guerra, I., Iannaccone, G., Mirabile, L., Vilardo, G., 1996. Seimic evidence for a low-velocity zone in the upper crust beneath Mount Vesuvuis. Science 274, 592–594.